

Mixed convection in turbulent channels with unstable stratification

SERGIO PIROZZOLI¹, MATTEO BERNARDINI¹,
ROBERTO VERZICCO^{2,3} AND PAOLO ORLANDI¹

¹Dipartimento di Ingegneria Meccanica e Aerospaziale, Sapienza Università di Roma
Via Eudossiana 18, 00184 Roma, Italy

²DII, Università di Roma Tor Vergata, Roma, Italy

³PoF, University of Twente, Enschede, The Netherlands

(Received 12 September 2016)

We study turbulent flows in planar channels with unstable thermal stratification, using direct numerical simulations in a wide range of Reynolds and Rayleigh numbers and reaching flow conditions which are representative of asymptotic developed turbulence. The combined effect of forced and free convection produces a peculiar pattern of quasi-streamwise rollers occupying the full channel thickness with aspect-ratio considerably higher than unity; it has been observed that they have an important redistributing effect on temperature and momentum. The mean values and the variances of the flow variables do not appear to follow Prandtl's scaling in the flow regime near free convection, except for the temperature and vertical velocity fluctuations, which are more affected by turbulent plumes. Nevertheless, we find that the Monin–Obukhov theory still yields a useful representation of the main flow features. In particular, the widely used Businger–Dyer relationships provide a convenient way of accounting for the bulk effects of shear and buoyancy, although individual profiles may vary widely from the alleged trends. Significant deviations are found in DNS with respect to the commonly used parametrization of the mean velocity in the light-wind regime, which may have important practical impact in models of atmospheric dynamics. Finally, for modelling purposes, we devise a set of empirical predictive formulas for the heat flux and friction coefficients which can be used with about 10% maximum error in a wide range of flow parameters.

1. Introduction

Mixed convection is the process whereby heat and momentum are transferred under the concurrent effect of shear and buoyancy, and it is at the heart of several physical phenomena of great practical importance, especially within the context of atmospheric dynamics. Flow stratification may be either of stable type (i.e. the higher layers are hotter than the lower), or unstable type (i.e. lower layers are heated). In the former case, stratification suppresses the vertical motions thus mitigating friction and heat transfer. In contrast, unstable stratification promotes turbulent exchanges with obvious opposite effects. Although the two extreme cases of pure forced convection (classical boundary layers and channel flows) and of free convection (Rayleigh–Bénard flow) have been extensively studied analytically, experimentally and numerically, their combination appears to be much less understood. The current engineering practice (Kays *et al.* 1980; Bergman *et al.* 2011) for heat transfer prediction in the presence of mixed convection mainly relies on correlations developed for either free or forced convection, and applied according to the value of

a global Richardson number, which grossly weights the effect of bulk buoyancy with respect to shear. However, combination of the two effects can give rise to flow patterns not recovered in either of the extreme cases. For instance, it is known (Avsec 1937; Hill 1968; Brown 1980) that in the presence of unstable stratification large streamwise-oriented rollers may form, which are regarded to be responsible for the formation of aligned patterns of strato-cumulus clouds (Mal 1930; Kuettner 1959, 1971), for the peculiar striped patterns in desert sand dunes with typical spanwise spacing of a few kilometers (Hanna 1969), and for the occurrence of long rows of unburned tree crowns in forest fires (Haines 1982). Wavy perturbations of the ordered pattern of convective rolls have also been frequently observed in the atmosphere (Avsec 1937; Avsec & Luntz 1937), and theoretically interpreted as the result of secondary instabilities (Clever & Busse 1991, 1992).

The current theoretical understanding of mixed convective flows heavily relies on the framework set up by Obukhov (1946); Monin & Obukhov (1954). Mainly based on dimensional arguments, the Monin-Obukhov theory relies on the existence of a universal length scale which incorporates the effects of friction and buoyancy, and defined as

$$L = \frac{u_\tau^3}{Q\beta g}, \quad (1.1)$$

where $u_\tau = \sqrt{\tau_w/\rho}$ is the friction velocity (with τ_w and ρ the time- and surface-averages wall viscous stress and the fluid density, respectively), Q is the total vertical heat flux, β is the thermal expansion coefficient of the fluid, and g is the gravity acceleration. It should be noted that the definition of equation (1.1) is consistent with that by Kader & Yaglom (1990), which specifically deals with the case of unstable stratification, although it slightly differs from the most common definition, which also includes a minus sign in front of the expression, and incorporates the Karman constant at the denominator. Given the definition of the Monin-Obukhov length scale, it is expected that for wall distances below L convection dominates and a logarithmic (like) dependence of the flow variables on the wall distance is observed. On the other hand, for distances from the wall beyond L buoyancy should dominate, with typical power-law scalings, to be discussed afterwards. The theory is frequently used in the meteorological context to estimate stress and heat flux from mean velocity and temperature gradients (Stull 2012), and in large-eddy-simulation (LES) as a wall function for enforcement of numerical boundary conditions at off-wall locations (Deardorff 1972). The Monin-Obukhov theory has received substantial experimental confirmation from atmospheric field measurements although with a large degree of scatter owing to inherent measurement uncertainties, and even certain basic features as the asymptotic mean velocity and temperature scalings under light-wind conditions are the subject of current controversy (Rao 2004; Rao & Narasimha 2006). Numerical support for Monin-Obukhov theory is to date rather scarce and it mainly comes from the large-eddy-simulation (LES) studies by Khanna & Brasseur (1997, 1998); Johansson *et al.* (2001), which raised issues regarding the proper scaling of horizontal velocity fluctuations. It is worthwhile noting that those LES studies were carried out at realistic atmospheric conditions, hence possibly affected by approximate sub-grid-scale parametrization as well as by uncertainties incurred with the use of Monin-Obukhov scaling to model the near-ground flow. To our knowledge, the Monin-Obukhov theory has never been systematically scrutinized through direct numerical simulation (DNS) and this is the main motivation of our study.

The channel flow is probably the most prototypical wall-bounded shear flow, and it has been extensively studied through DNS shed light on several important facets of wall turbulence structure. In particular, recent numerical studies have highlighted devi-

ations from the alleged universal behavior of wall turbulence associated with high-Re effects (Bernardini *et al.* 2014; Lee & Moser 2015). DNS studies have also addressed the behaviour of passive scalars transported by the fluid phase, which serve to model dispersion of dilute contaminants as well as turbulent thermal transport under the assumption of small temperature differences. The latest studies (Pirozzoli *et al.* 2016) have achieved a friction Reynolds number $Re_\tau \approx 4000$ (here $Ra_\tau = u_\tau h/\nu$, where h is the channel half-height) hence making it possible to establish the presence of a generalized logarithmic layer for the mean scalar profiles although with a slightly different set of constants than those of the streamwise velocity. Classical predictive formulas for heat transfer based on the log law (Kader 1981) are found to work quite well, with a suitable choice of the constants.

At the opposite side of the flow parameter range the Rayleigh-Bénard flow, corresponding to free convection between isothermal walls, has been extensively studied, both experimentally and numerically, mainly in cylindrical confined configurations (Ahlers *et al.* 2009). Rayleigh numbers up to 10^{15} have been reached experimentally (Niemela *et al.* 2000; Ahlers *et al.* 2012) while fully resolved numerical simulations are behind at $Ra = 2 \times 10^{12}$ (Stevens *et al.* 2011); around $Ra = 10^{14}$ the boundary layers adjacent to the heated plates become turbulent, and a transition to a state of ultimate convection is expected, marking a change from the classical $Nu \sim Ra^{1/3}$ behaviour to a steeper $\sim Ra^{(1/2)}/\ln(Ra^{3/2})$ ($\simeq Ra^{0.38}$ at $Ra = 10^{14}$). Attempts are ongoing to push the Rayleigh number of the simulations beyond $Ra = 2 \times 10^{12}$ since the experimental evidence in the ultimate regime is not unanimous and reliable numerical simulations would help solving the controversy. Pure Rayleigh-Bénard flow in planar geometry has to date received less attention, probably because of the lack of matching experimental data, and uncertainties related to potential dependence on the wall-parallel computational box size (Hamman & Moin 2015), the most notable example dating back to Kerr (1996). Recent numerical simulations of Rayleigh-Bénard flow in planar geometry in the presence of wall roughness and including the effect of finite thermal conduction at the walls have been carried out by Orlandi *et al.* (2015*b*).

Numerical simulations and experiments of internal flows in the presence of buoyancy have been relatively infrequent so far. Channel flows with stable temperature stratification have received some attention in recent years, with important contributions from DNS delivered by Armenio & Sarkar (2002); Garcia-Villalba & Alamo (2011), leading to the conclusion that flow relaminarization in the channel core may be achieved depending on the value of the bulk Richardson number. However, as pointed out by Garcia-Villalba & Alamo (2011), this effect sensitively depends on the size of the computational box, and extremely large domains are required to achieve box-independent results, even for the lowest order statistics. Channels with unstable stratification were considered in the experiments of Mizushima *et al.* (1982); Fukui & Nakajima (1985), which showed that for strongly unstable stratification the flow pattern is radically different than in the neutrally buoyant case, owing to the onset of quasi-longitudinal rollers which make up for large part of momentum and heat transfer. In one of the few quantitative measurements (Fukui *et al.* 1991) it was found that the typical size of each roller is about 1.3 times the channel height, although the aspect ratio of the duct was about 7, hence effects are likely to be significant. The formation of longitudinal rollers in turbulent flows was first confirmed in the DNS of Domaradzki & Metcalfe (1988), which however was dealing with Couette flow between sliding plates. Iida & Kasagi (1997) carried out numerical simulations of plane channel flows with unstable stratification at low bulk Richardson numbers ($Ri_b \leq 0.3$) and low Reynolds number ($Re_\tau = 150$), finding steady increase of the Nusselt number with Ri_b , whereas (quite interestingly) the friction coefficient was

found to slightly decrease up to $Ri_b \approx 0.05$. Sid *et al.* (2015) extended the envelope of the flow parameters to $Re_\tau \lesssim 400$, $Ri_b \lesssim 1$, confirming the non-monotonic trend of friction, and observing a typical blunting of the velocity and temperature profiles as the effect of buoyancy becomes significant. Using a DNS database at $Re_\tau \lesssim 200$, $Ra \lesssim 10^7$, Scagliarini *et al.* (2015) developed a phenomenological model resulting in a modified logarithmic law for the mean velocity which incorporates the effects of shear and buoyancy. Non-Oberbeck-Boussinesq effects associated with temperature dependent fluid properties were also studied by Zonta & Soldati (2014). Notably, all the above numerical studies were carried out at rather low Reynolds and/or Rayleigh number, hence they are not necessarily representative of fully turbulent flow conditions of practical relevance, and they span a limited range of Richardson numbers, typically close to the case of pure forced convection. Further, with the exception of the work of Zonta & Soldati (2014), simulations have been mainly carried out in narrow channels, which may prevent natural self-organization of large-scale coherent structures, as shown in recent studies on box size sensitivity (Hamman & Moin 2015). In fact, linear stability analysis (Gage & Reid 1968) predicts the onset on exponentially growing disturbances in the form of longitudinal rolls in the presence of unstable stratification, even at very low Rayleigh number. The most unstable disturbances predicted by linear stability analysis have a typical spanwise wavelength of about $4h$, which is comparable with the typical wavelength of the rollers recovered in fully turbulent simulations. Hence, $L_z = 4h$ may be regarded as a minimal spanwise box size to achieve healthy turbulence in channel flow simulations of mixed convection.

It is the main purpose of this study to establish a high-fidelity database for unstably buoyant channel flows which encompasses a wide range of Richardson numbers, at high enough values of Reynolds and Rayleigh number to be representative of fully developed turbulence. The numerical database is presented in §2, the flow organization is discussed in §3, and the main flow statistics in §4. The implications of the present findings in the light of Monin-Obukhov theory are discussed in §5, and considerations on heat transfer and friction predictive formulas are given in §6.

2. The numerical database

The Navier-Stokes equations for an incompressible buoyant fluid under the Boussinesq approximation are numerically solved

$$\frac{\partial u_j}{\partial x_j} = 0, \quad \frac{\partial u_i}{\partial t} + \frac{\partial u_i u_j}{\partial x_j} = -\frac{\partial p}{\partial x_i} + \beta g \theta \delta_{i2} + \Pi \delta_{i1} + \nu \frac{\partial^2 u_i}{\partial x_j \partial x_j}, \quad (2.1)$$

$$\frac{\partial \theta}{\partial t} + \frac{\partial \theta u_j}{\partial x_j} = \alpha \frac{\partial^2 \theta}{\partial x_j \partial x_j}, \quad (2.2)$$

where u_i are the Cartesian velocity components ($i = 1, 2, 3$ corresponding, respectively to the streamwise, wall-normal, and spanwise directions), θ is the temperature perturbation with respect to a reference state of hydrostatic equilibrium, β is the thermal expansion coefficient, g is the gravity acceleration, $\Pi = u_\tau^2/h$ is the forcing acceleration used to maintain a constant mass flow rate, and ν and α are the kinematic viscosity and temperature diffusivity, respectively. For that purpose, an existing channel flow solver with passive scalar transport (Pirozzoli *et al.* 2016) has been modified; the code is capable to discretely preserve the total kinetic energy and the scalar variance in the limit of vanishing diffusivities and time integration error.

The present flow is controlled by three global parameters, namely the bulk Reynolds

Flow case	Re_b	Ra	Ri_b	h/L	Re_τ	Nu	C_f	N_x	N_y	N_z
RUN_Ra9_Re0	0	10^9	∞	∞	0	63.172	NA	6144	768	3072
RUN_Ra9_Re4.5	31623	10^9	1	4.44264	946.41	60.255	7.16E-3	6144	768	3072
RUN_Ra8_Re0	0	10^8	∞	∞	0	30.644	NA	2560	512	1280
RUN_Ra8_Re3	1000	10^8	100	214.136	96.166	30.470	7.39E-2	2560	512	1280
RUN_Ra8_Re3.5	3162	10^8	10	30.0932	179.12	27.672	2.56E-2	2560	512	1280
RUN_Ra8_Re4	10000	10^8	1	3.67709	351.01	25.443	9.85E-3	2560	512	1280
RUN_Ra8_Re4.5	31623	10^8	0.1	0.44134	864.24	45.584	5.97E-3	2560	512	1280
RUN_Ra7_Re0	0	10^7	∞	∞	0	15.799	NA	1024	256	512
RUN_Ra7_Re2.5	316.2	10^7	100	167.716	38.690	15.541	1.20E-1	1024	256	512
RUN_Ra7_Re3	1000	10^7	10	24.4576	70.992	14.000	4.03E-2	1024	256	512
RUN_Ra7_Re3.5	3162	10^7	1	3.01888	134.98	11.880	1.46E-2	1024	256	512
RUN_Ra7_Re3.5_LA	3162	10^7	1	2.99729	136.12	12.094	1.48E-2	2048	256	1024
RUN_Ra7_Re3.5_SM	3162	10^7	1	2.85494	136.60	11.642	1.49E-2	512	256	256
RUN_Ra7_Re3.5_NA	3162	10^7	1	2.50569	142.59	11.622	1.62E-2	256	256	128
RUN_Ra7_Re4	10000	10^7	0.1	0.37257	307.01	17.250	7.54E-3	1024	256	512
RUN_Ra7_Re4.5	31623	10^7	0.01	0.04243	823.19	37.871	5.42E-3	2560	512	1280
RUN_Ra6_Re0	0	10^6	∞	∞	0	8.2884	NA	512	192	256
RUN_Ra6_Re2	100	10^6	100	114.745	16.436	8.1528	2.16E-1	512	192	256
RUN_Ra6_Re2.5	316.2	10^6	10	16.0776	30.527	7.3180	7.45E-2	512	192	256
RUN_Ra6_Re3	1000	10^6	1	1.94472	58.894	6.3560	2.77E-2	512	192	256
RUN_Ra6_Re3.5	3162	10^6	0.1	0.29783	112.47	6.7801	1.02E-2	512	192	256
RUN_Ra6_Re4	10000	10^6	0.01	0.02906	298.92	12.419	7.15E-3	1024	256	512
RUN_Ra6_Re4.5	31623	10^6	0.001	0.00349	817.63	30.508	5.35E-3	2560	512	1280
RUN_Ra5_Re3.5	3162	10^5	0.01	0.02262	108.48	4.6190	9.41E-3	512	192	256
RUN_Ra5_Re4	10000	10^5	0.001	0.00284	297.86	12.013	7.10E-3	1024	256	512
RUN_Ra4_Re3	1000	10^4	0.01	0.01508	45.731	2.3073	1.67E-2	512	192	256
RUN_Ra4_Re3.5	3162	10^4	0.001	0.00225	107.22	4.4345	9.19E-3	512	192	256
RUN_Ra0_Re3.5	3162	0	0	0	106.78	4.4836	9.12E-3	512	192	256
RUN_Ra0_Re4	10000	0	0	0	297.78	12.009	7.09E-3	1024	256	512
RUN_Ra0_Re4.5	31623	0	0	0	815.60	29.757	5.32E-3	2560	512	1280

Table 1: List of parameters for buoyant turbulent channel DNS. $Re_b = 2hu_b/\nu$ is the bulk Reynolds number, $Re_\tau = hu_\tau/\nu$ is the friction Reynolds number, $Ri_b = 2\beta g\Delta\theta h/u_b^2$ is the bulk Richardson number, $Ra = \beta g\Delta\theta(2h)^3/(\alpha\nu)$ is the Rayleigh number, $Nu = 2hQ/(\alpha\Delta\theta)$ is the Nusselt number, $C_f = 2\tau_w/(\rho u_b^2)$ is the skin friction coefficient. N_x , N_y , N_z are the number of grid points in the streamwise, wall-normal, and spanwise directions. An error stretching function $y(\eta) = \text{erf}[a(\eta - 0.5)]/\text{erf}(0.5a)$, $a = 3.2$, $\eta = [-1, 1]$ has been used to cluster grid points in the wall-normal direction. All simulations are carried out in a $L_x \times L_z = 16h \times 8h$ box, except for those labeled as LA ($32h \times 16h$), SM ($8h \times 4h$), NA ($4h \times 2h$).

number $Re_b = 2hu_b/\nu$, where u_b is the channel bulk velocity, the Rayleigh number, $Ra = (8h^3\beta g\Delta\theta)/(\alpha\nu)$, and the Prandtl number, $Pr = \nu/\alpha$, where $\Delta\theta$ is the temperature difference across the two walls. The relative importance of gravity as compared to convection is quantified by the bulk Richardson number, $Ri_b = 2h\beta g\Delta\theta/u_b^2 = Ra/(Re_b^2 Pr)$. All the simulations have been carried out at unit Prandtl number, covering the range of Reynolds and Rayleigh numbers $0 \leq Re_b \leq 10^{4.5} = 31623$, $0 \leq Ra \leq 10^9$. The various

Re_b	Line type	Ra	Symbol type
0	0	□
$10^{2.5}$	- - - - -	10^5	△
10^3	- · - · -	10^6	▽
$10^{3.5}$	- · - · -	10^7	△
10^4	- - - - -	10^8	◇
$10^{4.5}$	—————	10^9	○

Table 2: Nomenclature of lines (indicating the value of Ra) and symbols (indicating the value of Re_b).

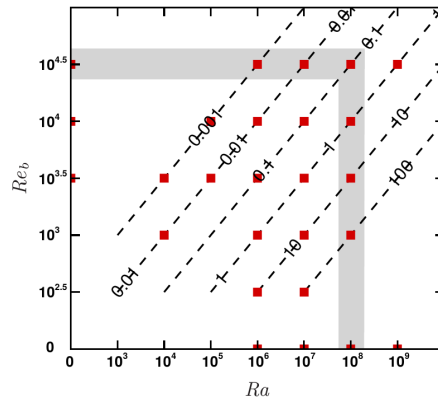


Figure 1: Overview of flow cases in the Ra - Re_b plane. Each solid square corresponds to a DNS. The dashed diagonal lines have constant Ri_b . The shaded area highlights the subset of DNS which have been mainly used for the statistical analysis. Note that the bi-logarithmic diagram is intentionally inconsistent for the purpose of including the extreme cases of free convection ($Re_b = 0$) and forced convection ($Ra = 0$).

DNS are labeled according to the following convention: RUN_Rax_Rey denotes a run carried out at $Ra = 10^x$, $Re_b = 10^y$, $Ra = 0$ corresponding to pure Poiseuille flow, and $Re_b = 0$ corresponding to pure Rayleigh-Bénard flow. Accordingly, the Richardson number may attain the extreme values 0 and ∞ , and finite values in the range $10^{-3} - 10^2$, in multiples of 10. An overview of the computed flow cases is presented in figure 1 in the Ra - Re_b plane. The extreme cases of Rayleigh-Bénard and Poiseuille flow are shown on the horizontal and vertical axes, respectively. It is important to note that in the chosen doubly-logarithmic representation the iso-lines of the bulk Richardson number are diagonal lines, and the flow conditions are selected in such a way that several flow cases are encountered along the iso- Ri_b lines to help isolate the effects of the parameters into play. Table 1 provides a list of the bulk flow parameters obtained for all the simulations herein carried out. The grid spacings have been carefully selected in such a way that the resolution requirements put forth by Shishkina *et al.* (2010) are satisfied in the limit case of pure buoyant flow, and the spacings in wall units are $\Delta x^+ = \Delta z^+ \lesssim 4.5$ in pure Poiseuille flow (Bernardini *et al.* 2014). The adequacy of the mesh resolution has been

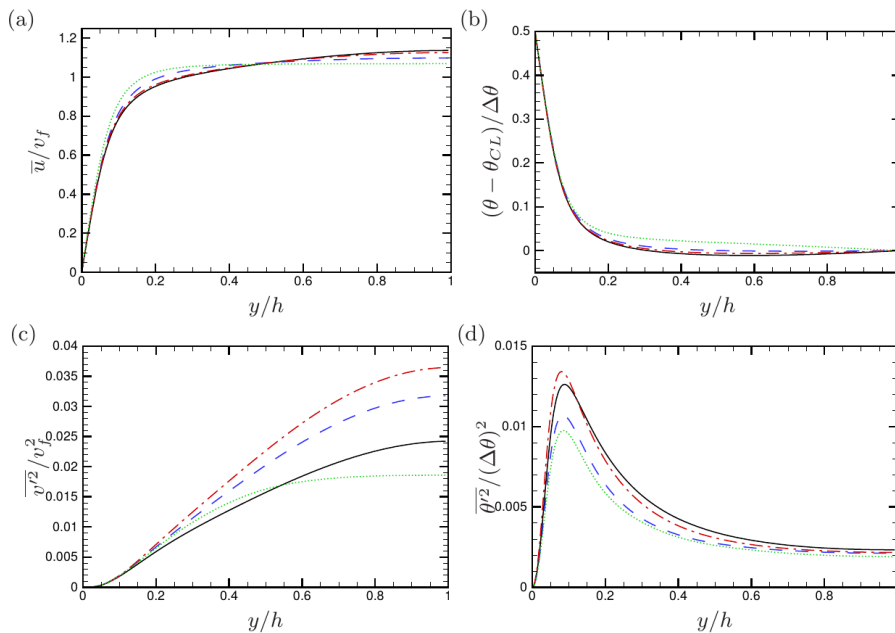


Figure 2: Sensitivity to computational box size for flow case RUN_Ra7_Re3.5 ($Ri_b = 1$): (a) mean velocity; (b) mean temperature; (c) variance of wall-normal velocity; (d) variance of temperature. $v_f = (2\beta gh\Delta\theta)^{1/2}$ is the reference free-fall velocity. Statistics are obtained in boxes with $L_x \times L_z = 4h \times 2h$ (dotted lines); $8h \times 4h$ (dashed lines); $16h \times 8h$ (solid lines); $32h \times 16h$ (dot-dashed lines).

checked a-posteriori for all the simulations, and the grid size in each coordinate direction is nowhere larger than three local Kolmogorov units.

Preliminary simulations have been carried out for flow case RUN_Ra7_Re3.5 (having $Ri_b = 1$) to establish the effect of computational box size on the turbulence statistics. The bulk flow parameters for these DNS, listed in table 1 suggest little effect of box size, except for the smallest box (having $L_x = 4h$, $L_z = 2h$), which shows symptoms of severe numerical confinement. Differences are clearer in the statistics of velocity and temperature, as shown in figure 2. The figure suggests that the computational domain has effects even on the mean flow properties, and especially the velocity variable that tends to have a flatter spatial distribution in narrow domains. Near insensitivity of mean velocity and temperature is observed starting at $L_x \times L_z = 16h \times 8h$, although velocity and temperature variances are still varying, even in non-monotonic fashion. Hence, given the need to keep the computational expense within reasonable bounds, and given the restrictions on the computational box size in Poiseuille flow (Bernardini *et al.* 2014), all simulations have been performed in a $16h \times 8h$ box.

For ease of later reference, the style of lines and symbols used to denote the various flow cases is explained in table 2. To avoid possible confusion it is important to note that, consistent with (most of) the wall turbulence community, the streamwise, wall-normal and spanwise coordinates are here labeled as x , y , z , respectively, and the corresponding velocity components as u , v , w . In contrast, in the geophysical community z and w are typically reserved for the vertical, wall normal, direction.

3. Flow organization

The flow structure is scrutinized in this section by analyzing instantaneous snapshots of the flow variables and their corresponding spectral densities. To get insights into the combined effects of Reynolds and Rayleigh numbers, we show velocity and temperature fluctuations (figures 3–5) in wall-parallel and cross-stream planes for several cases along the outer edge of the parameter-space matrix, marked with a shaded area in figure 1, for decreasing Ri_b . Specifically, DNS results are presented at constant $Ra = 10^8$ for increasing Re_b , up to $Ri_b = 1$, and then at constant $Re_b = 10^{4.5}$ for decreasing Ra , down to the limit case of Poiseuille flow. Two representative wall distances have been selected for the analysis; the channel centerline ($y = h$), where v' and θ' probe the large-scale flow organization, and the position of peak production of temperature fluctuations ($P_\theta = -\overline{v'\theta'}d\bar{\theta}/dy$), hereafter indicated as $y = y_P$, where we show u' and θ' . In the limit of free convection (panels (a)–(b)), persistent large-scale flow organization is observed at the channel centerline, consisting of a network of rollers which transport hot fluid from the bottom to the top (and vice versa) through upward- and downward-traveling plumes, as is evident from figure 5(a),(b). The flow visualizations suggest that the rollers have axes preferably pointing in the x and in the z direction, which is a likely consequence of the rectangular geometry of the computational domain. Indeed, the footprint of rollers with axes aligned in the z direction is apparent in the near-wall distribution of u (see figure 4a). As soon as the mean flow-rate becomes non-zero (panels (c)–(d), corresponding to $Ri_b = 100$), the flow attains a more definite spatial orientation, the rollers now mostly pointing in the streamwise direction. It is noteworthy that only two pairs of counter-rotating rollers are captured within the selected computational box. At intermediate Richardson numbers a strong meandering behavior of the rollers is observed, which is most evident at $Ri_b = 1$ (panels (e)–(f)), and which is the likely result of wavy instability of the counter-rotating rollers. This kind of instability is frequently observed in the meteorological context (Avsec 1937; Bénard & Avsec 1938), and in experiments (Pabiau *et al.* 2005), and it was theoretically explained in the context of laminar flow by Clever & Busse (1991). The association between vertical velocity and temperature fluctuations at the channel centreline, which well reflects the importance of vertical motions in the redistribution of the temperature field. Waviness of the rollers seems to be suppressed at further low Richardson number ($Ri_b = 0.01$, see panels g,h), at which the rollers are very nearly straight, and maximum organization is observed in cross-stream planes. Loss of coherence of the rollers and loss of correlation between v' and θ' is observed starting from $Ri = 0.001$ (panels (i)–(j)), which marks the passage to a spotty organization in the channel core typical of Poiseuille flow. In cross-stream planes (see figure 5), the change of regime from $Ri_b = 0.01$ to $Ri_b = 0.001$ is marked by the disappearance of rollers spanning the whole channel, although large eddies are still observed in the form of wall-attached ejections confined to each channel half (Bernardini *et al.* 2014).

As a result of the change in the bulk flow organization, the near-wall turbulence is also modified. In the case of free convection (figure 4(a)–(b)) the typical temperature pattern observed in Rayleigh-Bénard flow is recovered, with a distinctive network of near-wall line plumes protruding from the boundary layer into the bulk flow (Kerr 1996). A similar organization is found up to $Ri_b = 1$ (panels (e)–(f)), although a clear modulating influence from the overlaying rollers is found as the most intense near-wall plumes tend to be embedded within large-scale updrafts which are the ascending branch of core rollers (compare with figure 3(e)–(f)). In this regime the streamwise velocity does not have a definite small-scale organization, nor it is clearly associated with the temperature field. The scenario changes at $Ri_b = 0.01$ (figure 4(g)–(h)), with momentum streaks

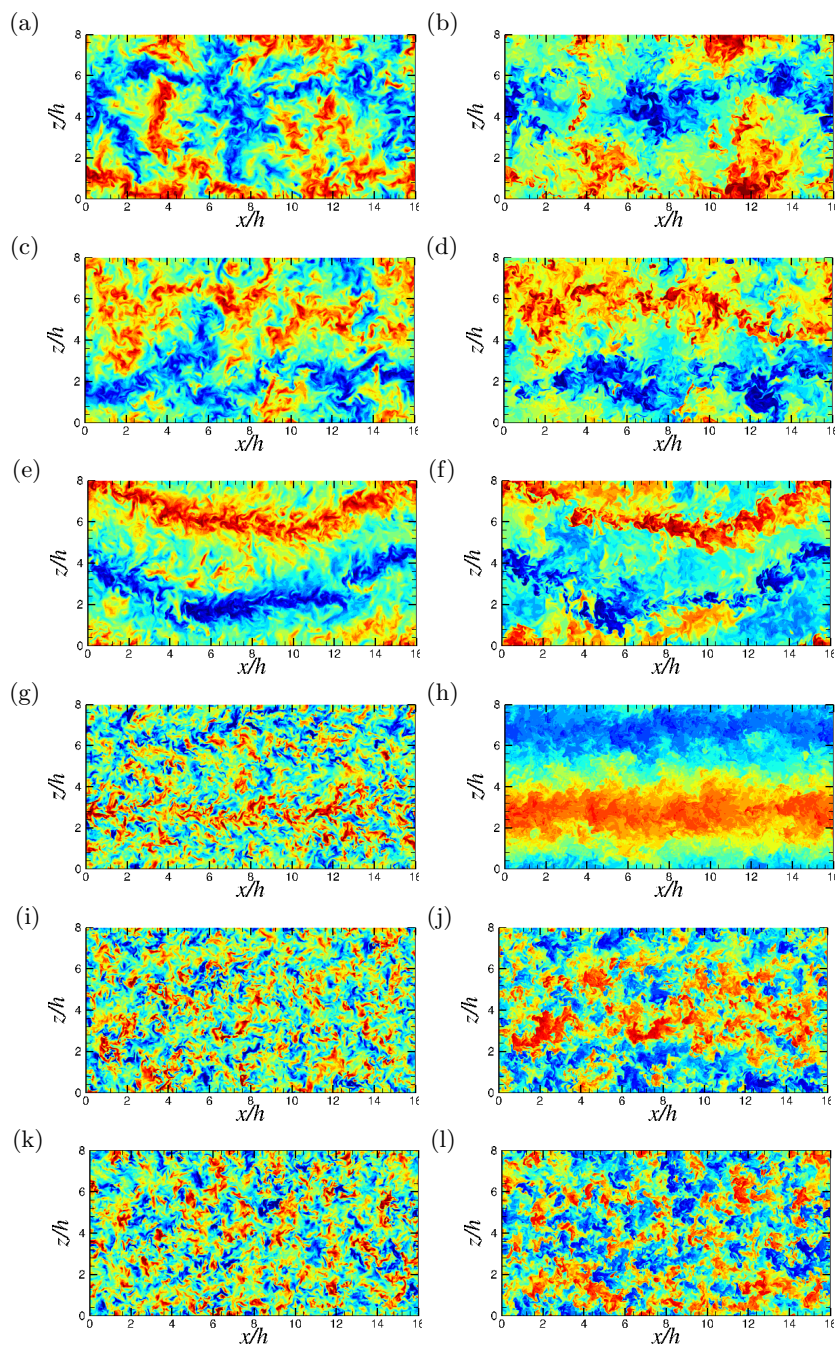


Figure 3: Effect of Reynolds and Rayleigh number variation: instantaneous visualizations of v' (left column) and θ' (right column) at channel center plane ($y = h$) for flow cases RUN_Ra8_Re0 ($Ri_b = \infty$, first row), RUN_Ra8_Re3 ($Ri_b = 100$, second row), RUN_Ra8_Re4 ($Ri_b = 1$, third row), RUN_Ra7_Re4.5 ($Ri_b = 0.01$, fourth row), RUN_Ra6_Re4.5 ($Ri_b = 0.001$, fifth row), RUN_Ra0_Re4.5 ($Ri_b = 0$, sixth row). 24 contour levels are shown for each variable in the range ± 3 standard deviations from the mean value (negative values in blue and positive in red).

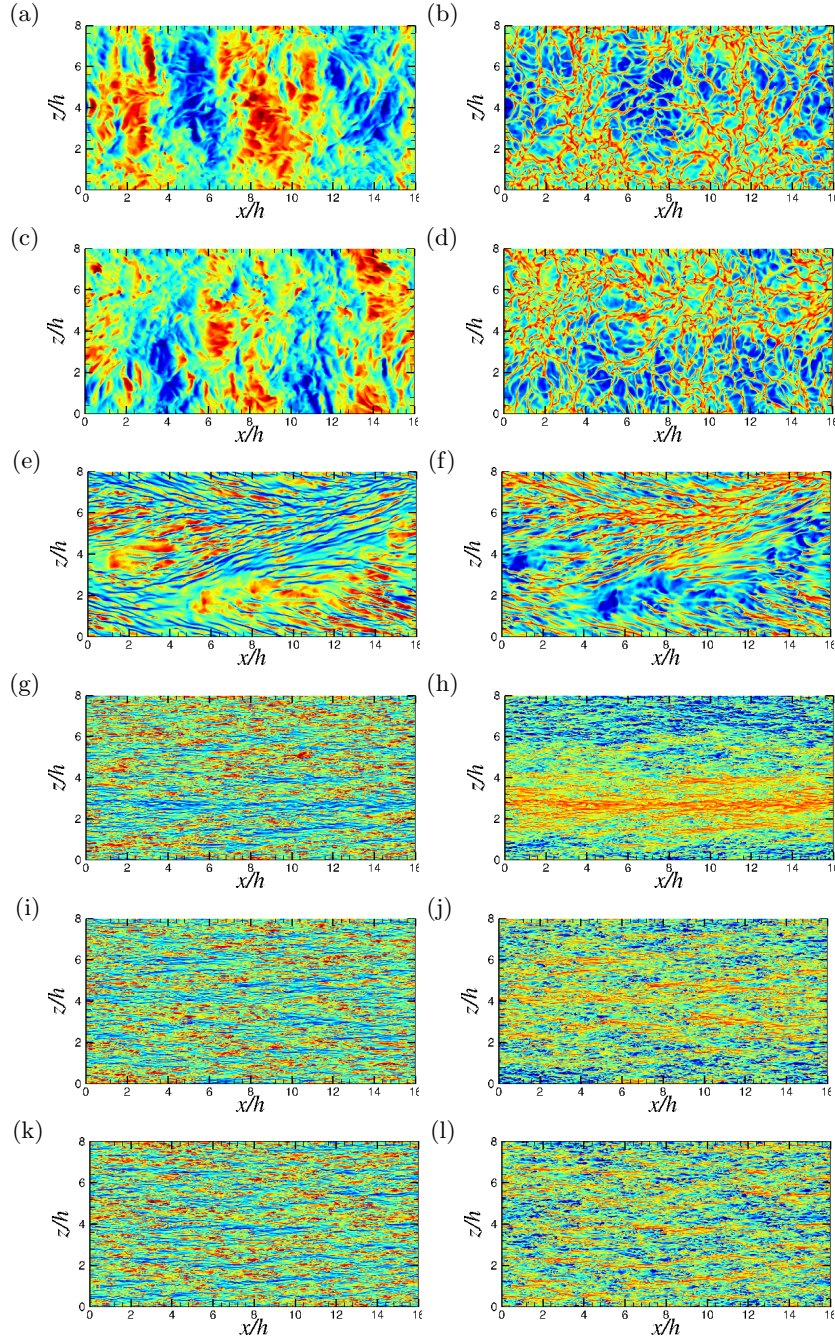


Figure 4: Effect of Reynolds and Rayleigh number variation: instantaneous visualizations of u' (left column) and θ' (right column) at near-wall station ($y = y_P$) for flow cases RUN_Ra8_Re0 ($Ri_b = \infty$, first row), RUN_Ra8_Re3 ($Ri_b = 100$, second row), RUN_Ra8_Re4 ($Ri_b = 1$, third row), RUN_Ra7_Re4.5 ($Ri_b = 0.01$, fourth row), RUN_Ra6_Re4.5 ($Ri_b = 0.001$, fifth row), RUN_Ra0_Re4.5 ($Ri_b = 0$, sixth row). 24 contour levels are shown for each variable in the range ± 3 standard deviations from the mean value (negative values in blue and positive in red).

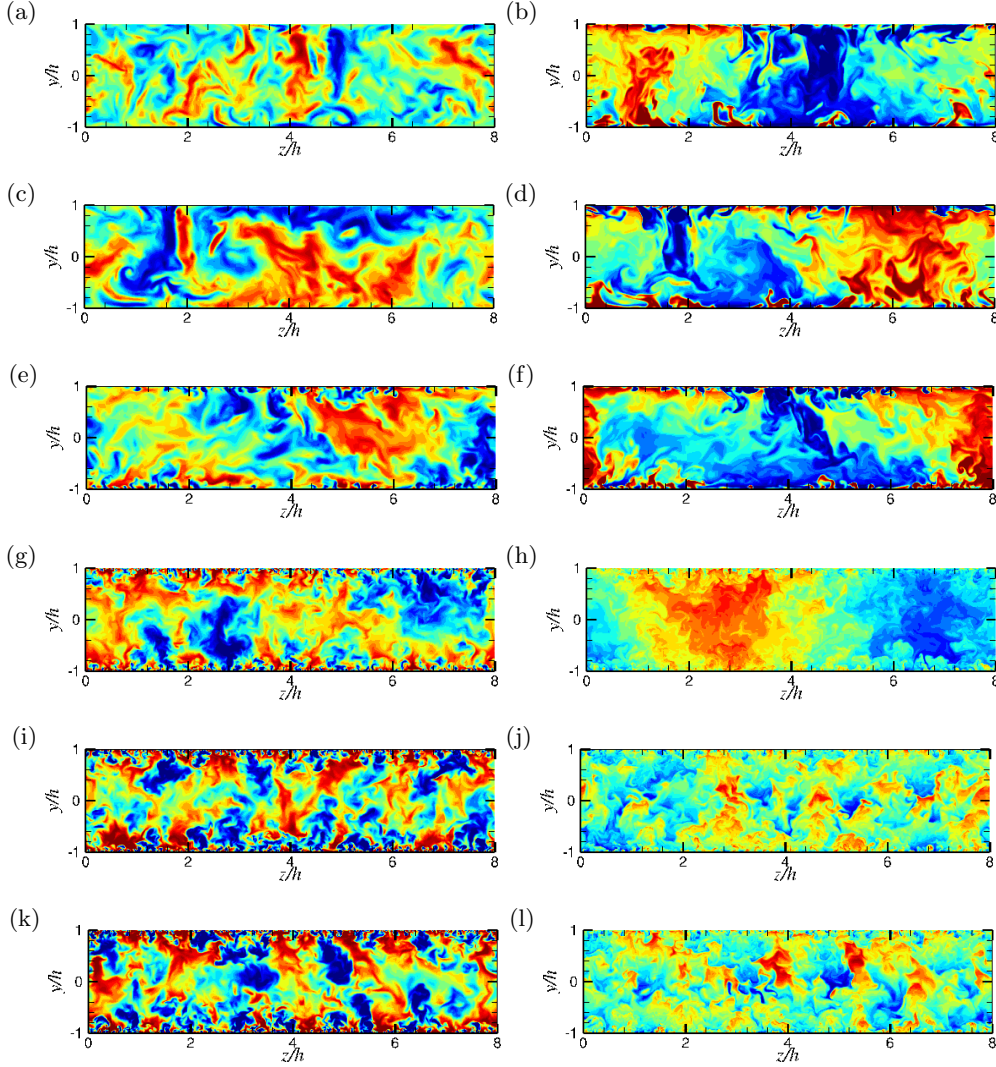


Figure 5: Effect of Reynolds and Rayleigh number variation: instantaneous visualizations of v' (left column) and θ' (right column) in cross-stream plane for flow cases RUN_Ra8_Re0 ($Ri_b = \infty$, first row), RUN_Ra8_Re3 ($Ri_b = 100$, second row), RUN_Ra8_Re4 ($Ri_b = 1$, third row), RUN_Ra7_Re4.5 ($Ri_b = 0.01$, fourth row), RUN_Ra6_Re4.5 ($Ri_b = 0.001$, fifth row), RUN_Ra0_Re4.5 ($Ri_b = 0$, sixth row). 24 contour levels are shown for each variable in the range ± 3 standard deviations from the mean value (negative values in blue and positive in red).

first appearing near the wall, which have strongly negative correlation with temperature fluctuations. At this Ri_b , the streaks appear to be strongly modulated by the action of the core rollers. However, as this action ceases ($Ri_b \leq 0.001$), near-wall turbulence attains the typical organization of canonical wall-bounded flows.

It is important to note that, to a first approximation, the type of flow pattern is controlled by the bulk Richardson number. As an illustrative example, in figure 6 we show flow visualizations for three flow cases with $Ri_b = 1$, in decreasing order of Re_b

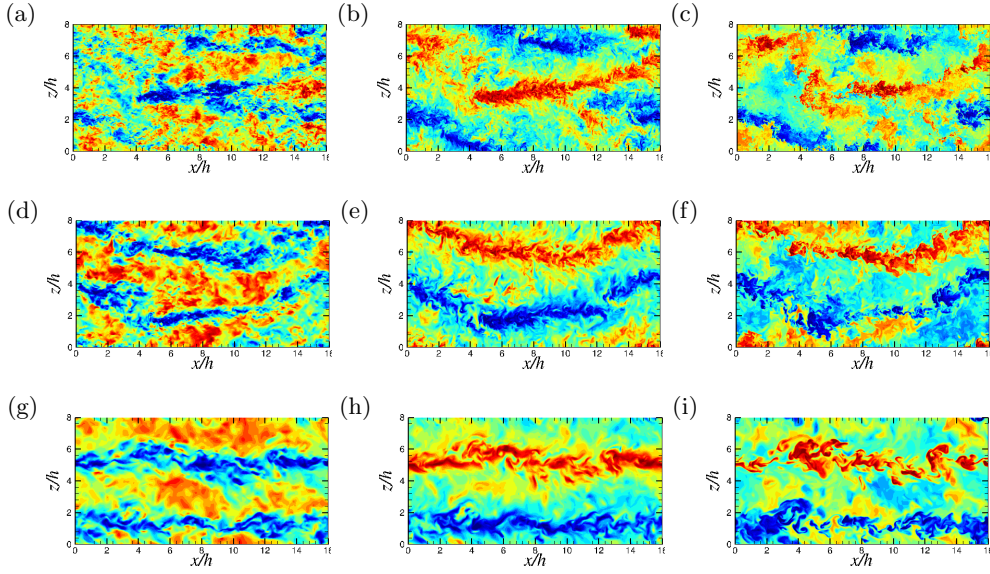


Figure 6: Numerical simulations at $Ri_b = 1$: instantaneous visualizations of u' (left column), v' (middle column), θ' (right column) at channel centerline for flow case RUN_Ra9_Re4.5 (first row), RUN_Ra8_Re4 (second row), RUN_Ra7_Re3.5 (third row). 24 contour levels are shown for each variable in the range ± 3 standard deviations from the mean value (negative values in blue and positive in red).

(and Ra). A similar type of large-scale organization is recovered in all three cases, perhaps with larger meandering of the rollers at the higher Re_b , at which finer scale organization of turbulence is obviously also observed.

More quantitative information regarding the flow structure can be gained by inspecting the spectral densities of the flow variables, providing information on the repartition of energy across the flow scales of turbulence. The spanwise spectra are here considered as they are not affected by bulk flow convection in the presence of shear (Bernardini *et al.* 2014). In figure 7(a) we show the spectra of wall-normal velocity fluctuations at the channel centerline in the classical Kolmogorov representation for all the flow cases shown in the previous flow visualizations, hence spanning the entire range of Richardson numbers. The figure shows near perfect universality of the distributions, and confirms adequate resolution of the small flow scales for all flow cases here reported. Excellent comparison is also obtained with transverse velocity spectra obtained from DNS data for isotropic turbulence (Jiménez *et al.* 1993), hence supporting universality of the small scales far from walls. To better highlight the different spatial organization at the large scales of motion, spectral densities of velocity components and temperature are shown in linear scale and as a function of the spanwise wavelength in panels (b)–(d). To rule out effects of large turbulence intensity variation with Re_b and Ra , the spectral densities are reported in normalized form (denoted with the hat symbol), in such a way that they all integrate to unity. The figure confirms the dominance of energetic motions spanning the full channel width. In fact, the most energetic Fourier mode for v and θ is found for all cases (with the exception of pure Poiseuille flow) at $\lambda_z = L_z$, which is consistent with the previously noticed occurrence of two rollers in all flow visualizations. It should be noted that the apparently non-monotonic Richardson number trend of the strength

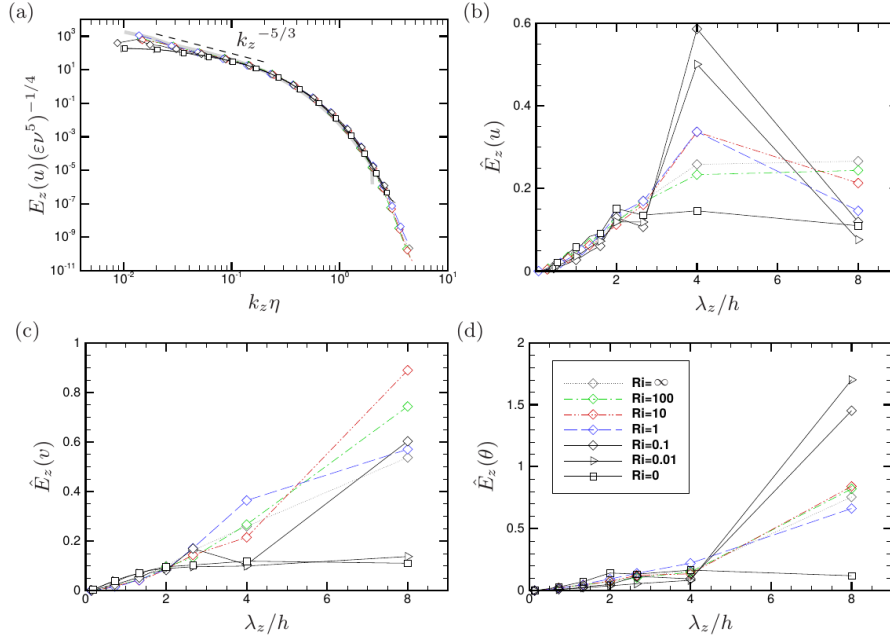


Figure 7: Spanwise spectral densities at channel centerline. In panel (a) the spectra of v' are shown in Kolmogorov representation (the thick grey line denotes the transverse velocity spectrum in isotropic turbulence at $Re_\lambda = 142$ (Jiménez *et al.* 1993)). In panels (b), (c), (d) we show the normalized spectra of u' , v' , θ' as a function of the wavelength. Refer to table 2 for nomenclature of lines and symbols.

of the L_z mode is due to the chosen normalization of the spectra. In fact, the unscaled spectra (not shown) have a monotonic increasing trend as Ri_b decreases. The behavior of the streamwise velocity spectra is quite different, and in that case the second Fourier mode ($\lambda_z = L_z/2$) is dominant, attaining a peak at $Ri_b = 0.1$. It is noteworthy that the doubled typical wavelength of u with respect to v is also different than observed in similar flows as plane Couette flow (Pirozzoli *et al.* 2014). The difference is due to the even symmetry properties of the mean velocity field with respect to the centerline, which implies that both upward and downward vertical motions locally convey positive streamwise velocity fluctuations. Hence, to each peak of v' at the channel centerline, two peaks of u' must be present.

The spectral densities at the near-wall station ($y = y_P$) are shown in figure 8. In this case, a semi-logarithmic representation is used for the pre-multiplied spectra, in such a way that equal areas correspond to equal energies. In flow cases near the free-convection limit the spectra of v and θ are bump-shaped, with a maximum at $\lambda_x \approx 0.3h$, which is connected with the typical spacing between adjacent near-wall plumes. On the other hand, the u and w spectra feature energy concentration at the largest scales, which is the footprint of the rollers sweeping the walls by horizontal ‘winds’ because of the impermeability condition. A change of behavior is noticed around $Ri_b = 1$, which marks a substantial reduction of the typical length scale of the v -bearing eddies towards $\lambda_z \approx 0.07h$, which corresponds to about 50 wall units (see table 1). This is the typical scale found in the near-wall streaks in Poiseuille flow (Kim *et al.* 1987), hence this change of flow scales is the symptom of passage from the regime of free to forced convection. A

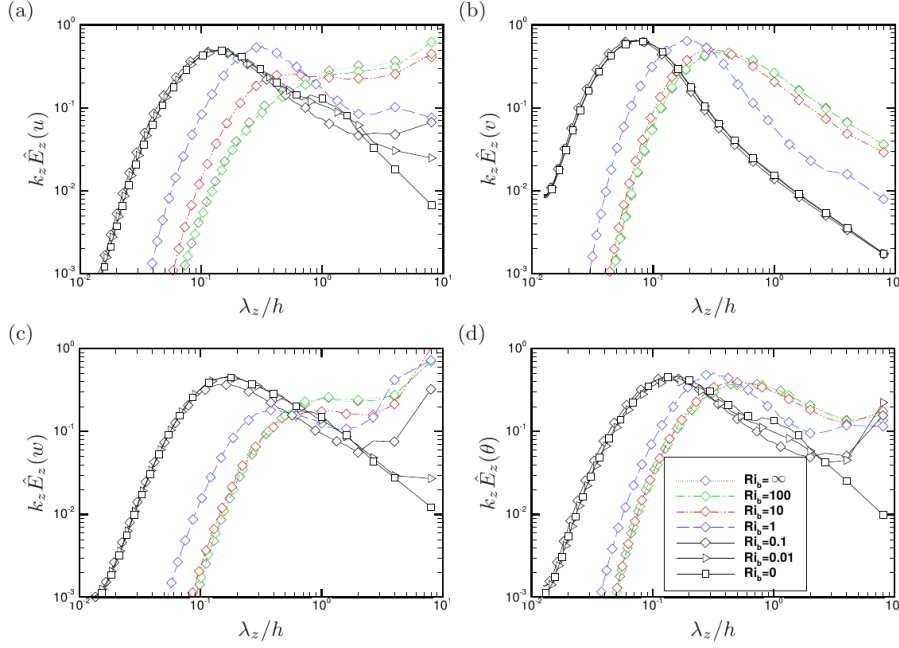


Figure 8: Pre-multiplied, normalized spanwise spectral densities of longitudinal velocity (a), vertical velocity (b), spanwise velocity (c) and temperature (c) at $y = y_P$.

bump also forms in the spectra of u , w and θ at $Ri_b \lesssim 1$, corresponding to about 100 wall units, again consistent with the behavior in Poiseuille flow. Notably, at intermediate Richardson numbers, the spectra of w' seem to contain more energy at the largest resolved modes than the spectra of u' , which can be explained recalling the dominant streamwise alignment of the rollers in the intermediate Ri_b regime.

4. Flow statistics

The main flow statistics are presented in this section, starting from the limiting cases of pure free and forced convection. The results obtained for Rayleigh–Bénard convection are shown at several Rayleigh numbers in figure 9, with temperatures scaled by the total difference $\Delta\theta$, and velocities scaled with the reference free-fall velocity $v_f = (2\beta gh\Delta\theta)^{1/2}$. For the sake of comparison of statistics at different Rayleigh numbers, wall distances (with the exception of panel (d)) are multiplied by the respective Nusselt number, as h/Nu is proportional to the thermal boundary layer thickness (Ahlers *et al.* 2009). In fact, the mean temperature profiles in panel (a) show near collapse in this representation, with an extended nearly linear profile, consistent with the established motion that at the (relatively low) Rayleigh numbers under scrutiny the boundary layer is in a (quasi-)laminar state (Ahlers *et al.* 2009). The location $y = h/Nu$ also very well matches the location where temperature fluctuations have a maximum (panel (b)), and the peak location of θ' production (namely y_P). It is noteworthy that the amplitude of this maximum depends on the Rayleigh number to some extent, with possible saturation at sufficiently high Ra . This effect is likely caused by the decreased amplitude of vertical motions when measured in v_f units (panel (d)), which also show evidence for saturation at high Ra . Apparently, saturation of θ' in confined geometries is not observed at Reyleigh numbers as high as

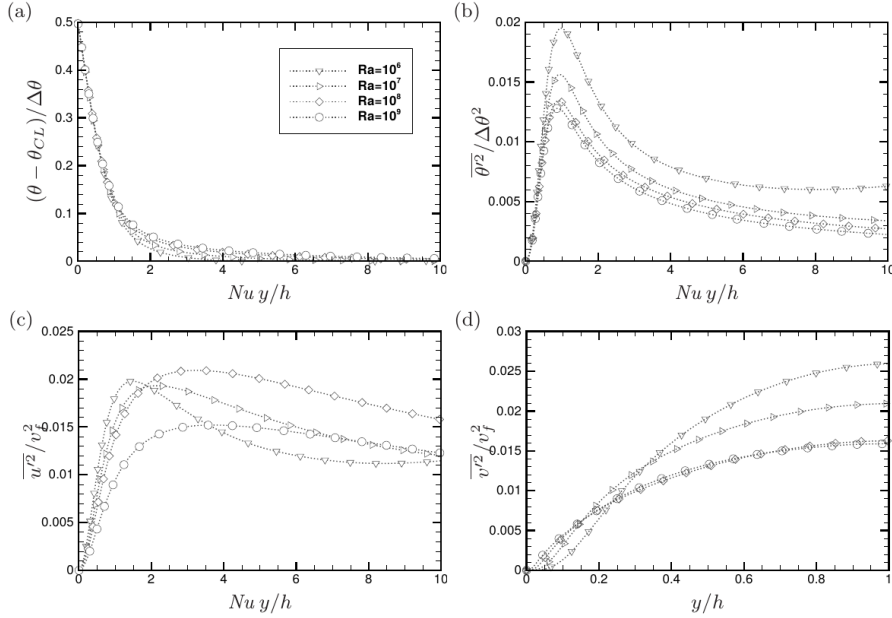


Figure 9: Profiles of mean temperature (a), temperature variance (b), horizontal velocity variance (c), and vertical velocity variance (d) in pure Rayleigh-Bénard flow ($Ri_b = \infty$). $v_f = (2\beta gh\Delta\theta)^{1/2}$ is the reference free-fall velocity, and the subscript CL is used to indicate the channel centerline state.

10^{11} (Stevens *et al.* 2011). Similar observations were made by Orlandi *et al.* (2015a), who noticed that in pure shear flow turbulent fluctuations (as compared to the bulk channel velocity) are in fact higher at lower Reynolds number. No systematic trend with Ra is observed for the horizontal velocity fluctuations (panel (c)), which are likely dominated by large-scale sweeping motions.

The structure of the velocity and temperature fields in natural convection has been the subject of extensive speculations within the meteorological community (Wyngaard 1992). It is a common notion that a free-convection layer exists in the atmosphere in which wind and temperature exhibit inverse power-law scalings with the wall distance

$$\begin{aligned} \frac{\bar{\theta}(y) - \theta_0}{\theta_\tau} &= 3B_\theta \left((y/L)^{-1/3} - (y_0/L)^{-1/3} \right), \\ \frac{\bar{u}(y) - u_0}{u_\tau} &= -3B_u \left((y/L)^{-1/3} - (y_0/L)^{-1/3} \right), \end{aligned} \quad (4.1)$$

where $\theta_\tau = Q/u_\tau$ is the friction temperature, L is the Monin-Obukhov length scale defined in equation (1.1), the subscript 0 denotes a suitable off-wall reference location, and B_θ and B_u are two supposedly universal constants (Kader & Yaglom (1990) report $B_\theta \approx 1.3$, $B_u \approx 1.9$). Equation (4.1) was first derived by Prandtl (1932) from mixing length arguments, based on the assumption that the typical vertical velocity scale of buoyant plumes is $v_P = (\beta g Q y)^{1/3}$, the associated temperature scale is $\theta_P = Q^{2/3}(\beta g y)^{-1/3}$, and the turbulent Prandtl number is constant. Hence, the accompanying expectation for velocity fluctuations is that they grow as $y^{1/3}$, whereas temperature fluctuations should decay as $y^{-1/3}$. Atmospheric measurements (Kader & Yaglom 1990) suggest that the scaling laws (4.1) are grossly satisfied in the free-convection regime. However, field ex-

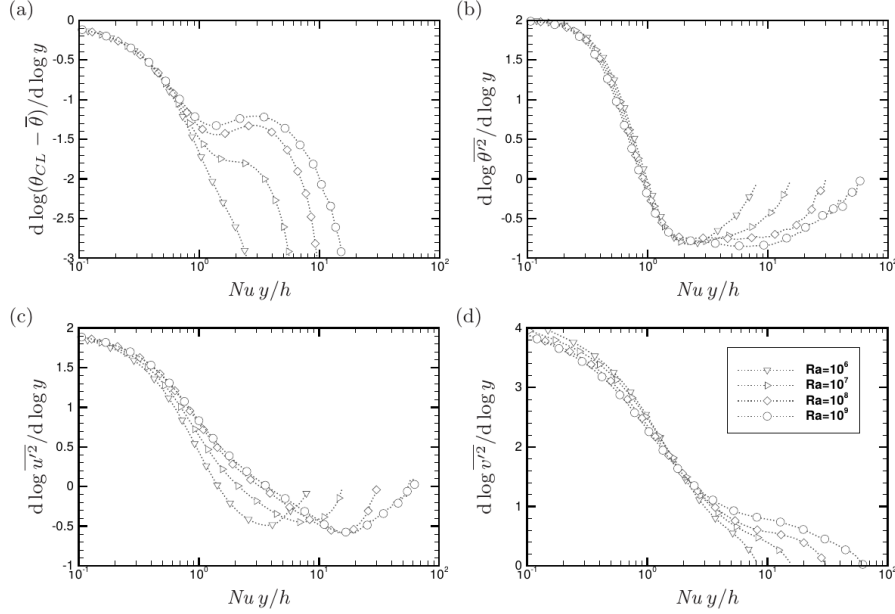


Figure 10: Power-law diagnostic functions for mean temperature (a) temperature variance (b), horizontal velocity variance (c), and vertical velocity variance (d), in Rayleigh-Bénard flow ($Ri_b = \infty$).

periments in that regime are inevitably affected by the presence of (albeit small) mean winds, which implies large uncertainties and lack of reproducibility. On the other hand, laboratory experiments of pure convection have mostly focused on strongly confined conditions (Ahlers *et al.* 2009), hence do not convey much useful information for the purpose. To directly verify the occurrence of the inverse power-law behaviour given by (4.1) in our DNS data we consider the distributions of the power-law indicator functions, defined as $\Xi_\varphi = (y/\varphi) d\varphi/dy$ for several flow variables. The presence of a plateau in Ξ_φ would obviously indicate a $\varphi \sim y^{\Xi_\varphi}$ power-law range. The power-law indicators for mean temperature and for velocity and temperature variances are shown in figure 10 for free convection flow cases. The mean temperature (panel (a)) does not show any evidence of a sensible layer with power-law behaviour. It may be argued that a dip is forming in a narrow range of wall distances at the highest Rayleigh number here considered ($Ra = 10^9$), although the resulting power-law exponent is far from the alleged $-1/3$. This large discrepancy with respect to the Prandtl's theory seriously puts into question the validity of the predicted scaling, or perhaps suggests that extreme Rayleigh numbers are required to observe the $y^{-1/3}$ law. On the other hand, it is found that an extended power-law region forms for the temperature fluctuations with exponent not far from the expected $-2/3$ value, and which widens with Ra . The situation is even less clear for the velocity fluctuations. Specifically, while the variance of vertical fluctuations may seem to form a small plateau with positive power-law exponent (optimistically, not far from the expected $2/3$), streamwise fluctuations are consistently decreasing towards the channel centerline, thus clearly contradicting the expected increasing trend. This odd behavior of velocity fluctuations in free convection has been long recognized, and deviations from Prandtl's scaling have been frequently attributed to the important effect of h -scaled eddies on the horizontal velocity components (Panofsky *et al.* 1977). Kader & Yaglom

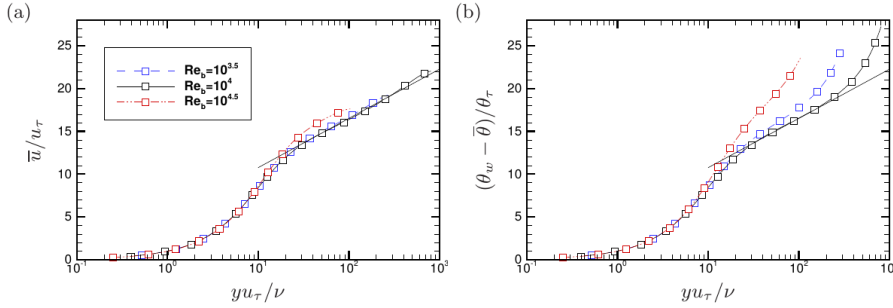


Figure 11: Profiles of mean streamwise velocity (a) and mean temperature (b) for pure Poiseuille flow ($Ri = 0$). The solid lines correspond to logarithmic laws for velocity and temperature.

(1990) also predicted a $y^{-2/3}$ scaling for the horizontal velocity variances, based on the assumption that the relevant velocity scale for horizontal velocity fluctuations is u_τ^2/ν_P . Our impression is that figure 10(c) at least partially confirms their prediction, although no extended power-law range is observed here.

In the sake of completeness the mean velocity and temperature profiles for the case of pure Poiseuille flow are also shown in figure 11. It is found that the mean velocity profiles (panel (a)) are accurately fitted using the conventional logarithmic approximation, namely $u/u_\tau = C + \log(yu_\tau/\nu)/k$, with the traditional choice $C = 5$, $k = 0.4$. The same approximation works well also for the temperature field (panel (b)), hence at unit Prandtl number and in the absence of coupling through buoyancy, very close similarity is found between the velocity and the temperature fields, except in the channel core, where temperature must have non-zero derivative.

The effect of Richardson number variation starting from the free-convection regime is illustrated in figure 12. As Ri_b decreases (i.e. the mass flow rate increases at given Ra) the mean temperature profile (a) tends to become less flat, departing from the free-convection distribution, and eventually attaining a near logarithmic distribution. The mean velocity profile (b) has a more complex behavior, initially becoming more blunted down to $Ri_b = 0.1$, and then less flat while approaching the Poiseuille limit. Although the bulk Reynolds number is very low in the light-wind (high- Ra) simulations, the velocity profile seems to be much different than the laminar Poiseuille profile, which is also shown in panel (b) for reference. For instance, the flow case RUN_Ra8_Re3 (corresponding to $Ri_b = 100$) shows a blunted profile despite having a bulk Reynolds number well below the expected threshold for forced turbulence to sustain itself in pure shear flow. This intermediate state is not found in either of the limit cases of Rayleigh-Bénard and Poiseuille flow, while having some features of both. Regarding the statistics of turbulent fluctuations (only shown here for $Ri_b \geq 0.1$ for clarity), a very similar pattern as in free convection is observed down to $Ri_b = 1$. A different regime starts at $Ri_b = 0.1$, which is associated with increased importance of shear. Hence, near-wall peaks of u' and v' form, and the profile of θ' tends to flatten in the channel core.

The same properties are reported upon wall scaling in figure 13, to highlight deviations from the forced convection limit at increasing Ri_b . In wall units, both the temperature and the velocity profiles approach the zero- Ri_b log-law limit from below, and logarithmic layers for both variables are observed starting at $Ri_b = 0.1$. A universal wall scaling for the velocity and temperature fluctuations is also established at $Ri_b = 0.1$, with near-wall peaks of u' and θ' at $y^+ \approx 15$, and peaks of v' and w' further away. At higher

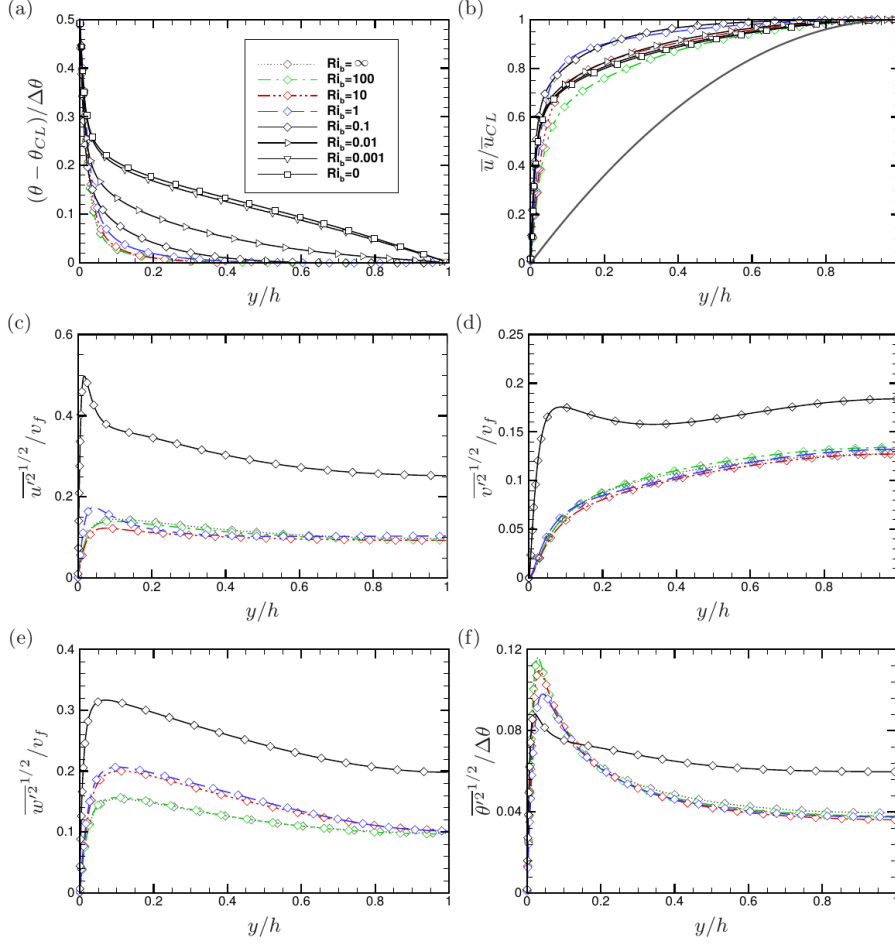


Figure 12: Profiles of mean temperature (a), mean streamwise velocity (b), streamwise velocity variance (c), vertical velocity variance (d), spanwise velocity variance (e) and temperature variance (f). The thick grey lines in panel (b) corresponds to the laminar Poiseuille parabolic profile.

Ri_b increasing values are found for the wall—scaled velocity fluctuations, and lower values are found for the temperature fluctuations. This is the result of a change from wall scaling to free—fall scaling, since here Re_b is decreasing at constant Ra , and as a result $v_f/u_\tau = \sqrt{Ra/Pr}/(2Re_\tau)$ is increasing, and $\theta_\tau/\Delta\theta$ is decreasing at increasing Ri_b . Furthermore, the peaks of u' and w' tend to come close to each other because of flow isotropization in wall—parallel planes.

Further insights into changes occurring between $Ri_b = 0.1$ and 1 can be gained from figure 14. In panel (a) we report the distributions of the flux Richardson number

$$Ri_f = \frac{-\beta g \overline{v'\theta'}}{\overline{u'v'} d\bar{u}/dy}, \quad (4.2)$$

representing the ratio of the production of vertical velocity variance to the production of horizontal velocity variance. Hence, Ri_f is expected to be a local indicator of the relative dynamical importance of buoyancy as compared to shear. Except for the limiting case of

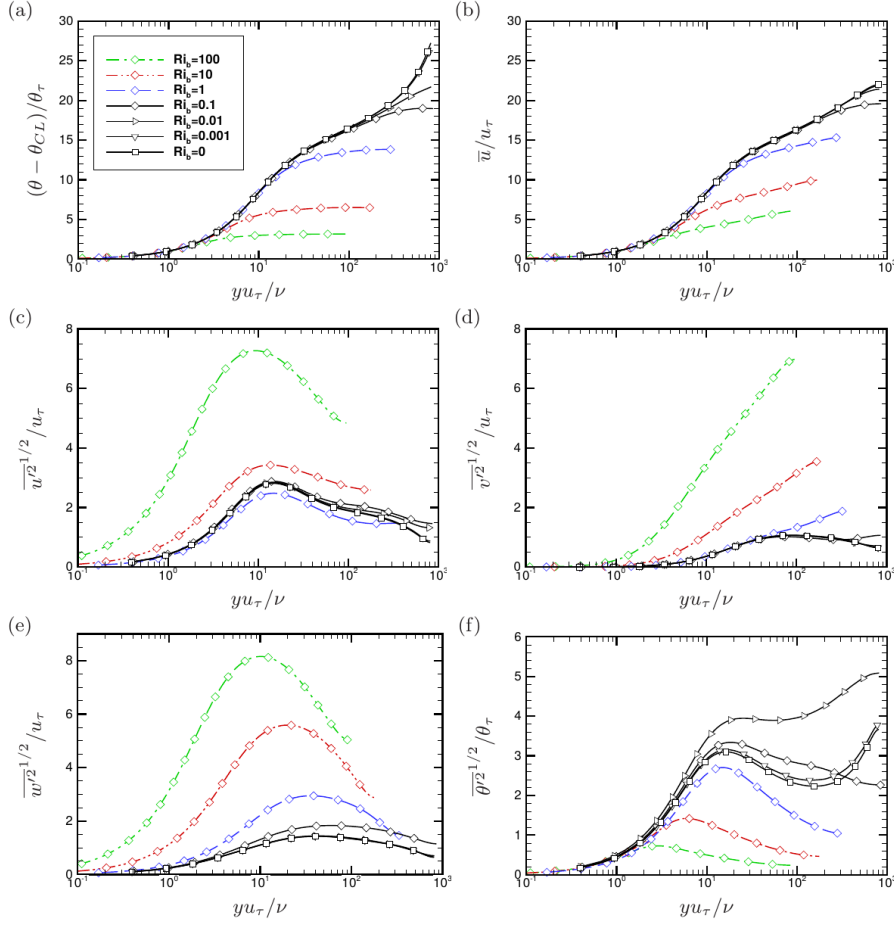


Figure 13: Shear-scaled profiles of mean temperature (a), mean streamwise velocity (b), streamwise velocity variance (c), vertical velocity variance (d), spanwise velocity variance (e) and temperature variance (f), in mixed convection regime.

high Ri_b , the near-wall region is always dominated by shear, hence it is referred to as dynamic or convective sublayer (Kader & Yaglom 1990) in the meteorological community. Further up, the flow in the so-called free-convection layer is dominated by buoyancy. A major change occurs between $Ri_b = 1$, where the dynamic sublayer occupies about 10% of the wall layer, and $Ri_b = 0.1$, where this fraction exceeds 50%. A quantity of great relevance in turbulence models for scalar transport is the turbulent Prandtl number, defined as the ratio of the turbulent momentum and temperature diffusivities, namely

$$Pr_t = \frac{\nu_t}{\alpha_t} = \frac{\overline{u'v'}}{\overline{v'\theta'}} \frac{d\bar{\theta}/dy}{d\bar{u}/dy}, \quad (4.3)$$

whose distribution is shown in figure 14(b). Consistently with numerical and experimental data (Cebeci & Bradshaw 1984; Kader 1981; Pirozzoli *et al.* 2016), in the forced convection regime Pr_t is close to unity in the near-wall region, and to 0.85 in the bulk flow up to $y/h \approx 0.5$. Notably, the Prandtl number starts dropping from the outer layer at $Ri_b = 0.01$, and its value is well below unity throughout the channel at high Ri_b .

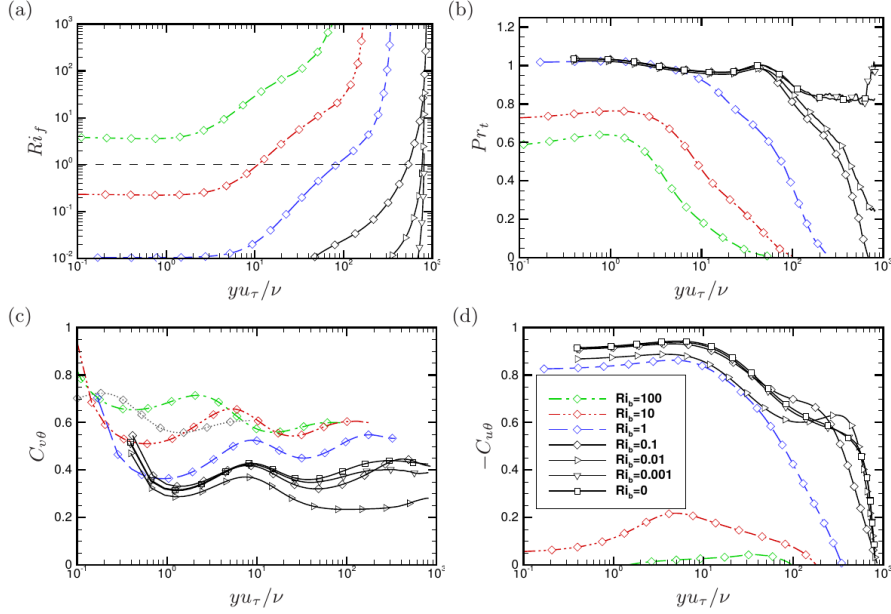


Figure 14: Profiles of flux Richardson number (a), turbulent Prandtl number (b), $v - \theta$ correlation coefficient (c) and $u - \theta$ correlation coefficient in the mixed convection regime. The dashed horizontal line in panel (a) marks the unit value of Ri_f .

This behaviour is in clear contradiction with the assumption of constant Pr_t advocated in Prandtl's free-fall theory, and it clearly indicates that buoyancy is much more effective in redistributing temperature than momentum. This behaviour is confirmed by the $v - \theta$ and $u - \theta$ correlation coefficients, shown in panels (c) and (d), respectively. As found in canonical Poseuille flow (Pirozzoli *et al.* 2016), $C_{v\theta}$ stays close to 0.4 throughout the wall layer at low Ri_b , and it increases with Ri_b reaching a value of about 0.6 in free convection, reflecting increased effectiveness of wall-normal motions. On the other hand, $C_{u\theta}$ (obviously negative) is found to be close to 0.9 near the wall and to decrease with the wall distance in forced convection, reflecting the similarity in the behavior of u with that of a passive scalar (Abe & Antonia 2009). The correlation drops sharply past $Ri_b = 1$, reflecting the change in the organization of u by buoyancy-induced vertical motions, presumably through pressure effects.

5. Monin-Obukhov scaling

A useful parametrization of the wall region in the presence of mixed convection is provided by the Monin-Obukhov theory (Obukhov 1946; Monin & Obukhov 1954). Starting from the assumption that the correct velocity scale in wall bounded flows is the friction velocity u_τ , and the only dimensionally correct length scale is L as defined in equation (1.1), the following scalings result for the fully turbulent part of the wall layer

$$\frac{y}{\theta_\tau} \frac{d\bar{\theta}}{dy} = \varphi_h \left(\frac{y}{L} \right), \quad \frac{y}{u_\tau} \frac{d\bar{u}}{dy} = \varphi_m \left(\frac{y}{L} \right), \quad (5.1)$$

$$\frac{\overline{u_i'^2}}{u_\tau} = \varphi_i \left(\frac{y}{L} \right), \quad \frac{\overline{\theta'^2}}{\theta_\tau} = \varphi_\theta \left(\frac{y}{L} \right), \quad \frac{-\overline{u'\theta'}}{Q} = \varphi_{u\theta} \left(\frac{y}{L} \right), \quad (5.2)$$

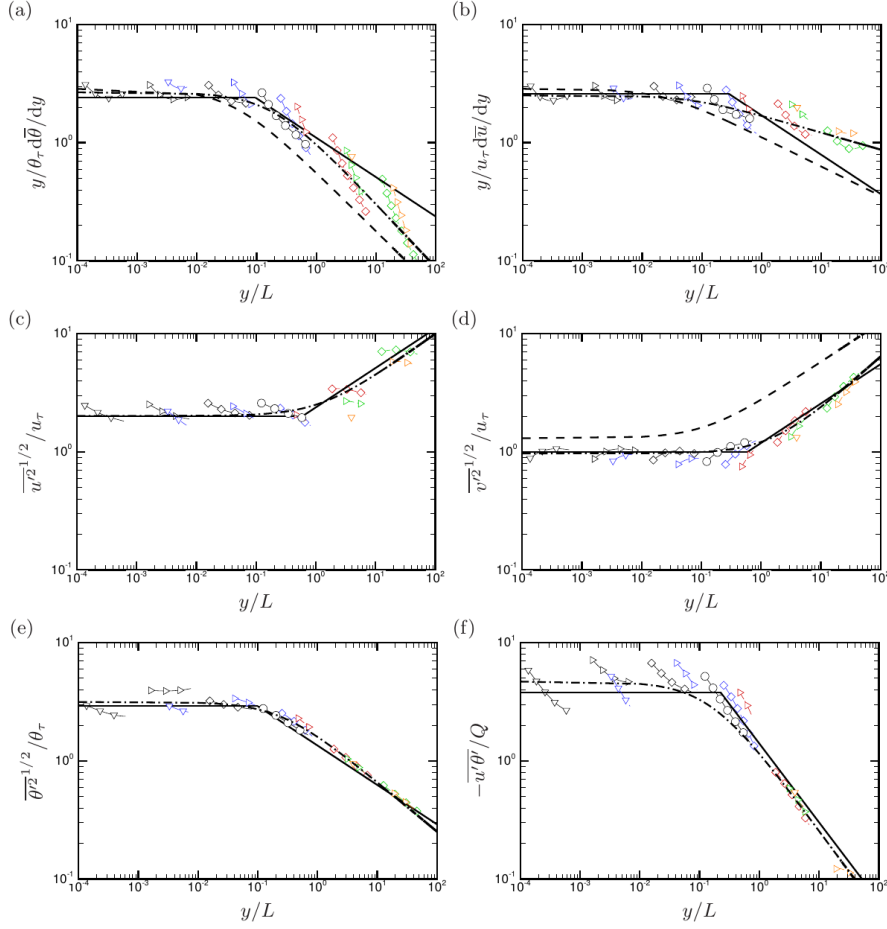


Figure 15: Verification of Monin-Obukhov similarity hypothesis for: (a) mean temperature gradient; (b) mean velocity gradient; (c) streamwise velocity variance; (d) vertical velocity variance; (e) temperature variance; (f) $u - \theta$ correlation. The solid lines indicate a compound of the scaling laws proposed by Kader & Yaglom (1990), the dashed lines denote the Businger-Dyer relationships with classical values of the constants, whereas the dot-dashed lines indicate a fit of the DNS data (see table 3). See table 2 for nomenclature of lines and symbols.

with $-\overline{u'v'} \approx \tau_w$, $-\overline{v'\theta'} \approx Q$ and the φ 's a suitable set of universal functions. The Monin-Obukhov relations are widely used in the meteorological practice and as wall functions in numerical simulations of atmospheric circulation as they allow to estimate momentum and temperature fluxes from mean flow gradients evaluated away from the wall (Deardorff 1970; Stull 2012). Regarding the choice of the universal functions, the typical approach (Kader & Yaglom 1990) consists of interpolating between the extreme conditions of forced and free convection. For instance, regarding the scaling of temperature, it is expected that in forced convection a logarithmic layer of $\bar{\theta}$ forms, hence $\varphi_h \approx k_\theta$, where k_θ is the Karman constant for passive scalars (Kader 1981). On the other hand, granted the validity of Prandtl's theory of free convection (as from equation (4.1)), the scaling $\varphi_h \sim (y/L)^{-1/3}$ would result. A frequently used representation for the universal func-

Quantity	k	γ	α	α_{KY}	α_{BDP}
φ_h	0.375	5.67	-0.538	-1/3	-1/2
φ_m	0.399	14.6	-0.145	-1/3	-1/4
φ_1	0.498	0.830	0.361	1/3	/
φ_2	1.03	0.638	0.452	1/3	1/3
φ_θ	0.318	4.08	-0.420	-1/3	/
$\varphi_{u\theta}$	0.214	6.70	-0.690	-2/3	/

Table 3: Coefficients of DNS data fits reported in figure 15, assuming functional dependence of the type $\varphi = 1/k(1 + \gamma y/L)^\alpha$. The coefficients α_{KY} denote the expected power-law scaling exponents in the free-convection regime predicted by Kader & Yaglom (1990), and the α_{BDP} those used in the classical Businger–Dyer and Panofsky relationships.

tions of Monin–Obukhov theory consists of the Businger–Dyer relationships (Businger *et al.* 1971; Dyer 1974), which assume

$$\varphi_h = \frac{1}{k_\theta} (1 + \gamma_h y/L)^{\alpha_h}, \quad \varphi_m = \frac{1}{k} (1 + \gamma_m y/L)^{\alpha_m}, \quad (5.3)$$

with the typical choice of constants (Paulson 1970) $k = k_\theta = 0.35$, $\gamma_m = \gamma_h = 16$, $\alpha_h = -1/2$, $\alpha_m = -1/4$. Hence, these relationships account for strong deviations of the mean temperature and velocity fields from the alleged $(y/L)^{-1/3}$ behavior in the limit of light winds. Similar empirical relations have been proposed for the vertical velocity variances by Panofsky *et al.* (1977), which are also included in the figure. In order to check the validity of the Monin–Obukhov similarity predictions, the DNS data are reported in scaled form in figure 15. For that purpose, data have been collected in a limited part of the wall layer, identified under the somehow arbitrary conditions that: i) the turbulent heat flux is higher than 90% of the total flux; ii) the turbulent momentum flux is higher than 90% of its maximum value. These conditions basically identify the assumptions made by the Monin–Obukhov theory that the viscous fluxes are negligible, and the total stress is approximately constant. In figure 15 we also show the asymptotic trends suggested by Kader & Yaglom (1990), as well as the results obtained by fitting the DNS data with Businger–Dyer–like distributions, with coefficients given in table 3. Panel (a) of figure 15 shows flat behaviour of the scaled temperature gradient up to $y/L \approx 0.1$, followed by a global roll-off with power-law exponent close to the $-1/2$ value given by the Businger–Dyer relationships, but sensibly steeper than the $-1/3$ value expected in free convection. It should also be noted that the individual profiles are far from following the predicted scalings, but rather tend to follow much sharper inverse power laws, as previously discussed in figure 10(a). Similar observations have been occasionally made in the literature (Khanna & Brasseur 1997), and attributed to the importance of h -scaled circulatory motions, which would imply the inclusion of h/L (commonly referred to as the stability parameter) as an additional parameter in the Monin–Obukhov functional relationships. Incidentally we note that, based on the present DNS data, the stability parameter is approximately a unique function of the bulk Richardson number, and we find $h/L \simeq 3.34 Ri_b^{0.85}$. The scaled mean velocity gradient (figure 15(b)) also has a flat behavior up to $y/L \approx 0.1$, with very slow roll-off, probably slower than the $(y/L)^{-1/4}$

given by the Businger–Dyer relationships, although the data scatter here is quite severe, and again individual profiles follow steeper power laws. As pointed out by Rao & Narasimha (2006), the parametrization of the velocity field in the presence of light wind under unstable stratification is a weak point of weather forecast models, mainly because field experiments typically convey large scatter for obvious difficulties in achieving stable flow conditions. For instance, based on field measurements, Kader & Yaglom (1990) even argue about possible inversion of the φ_m curve at high y/L , which however finds no support in our data. DNS is especially valuable as sustained flow conditions are achievable, although higher values of the Reynolds number would be clearly desirable. The velocity and temperature fluctuations (panels (c)–(e)) globally follow the Monin–Obukhov scalings quite well. Especially satisfactory is the behavior of the vertical velocity and temperature fluctuations in the light–wind regime, as previously noticed regarding the free–convection convection (see figure 10b,d). This finding probably points to the fact that vertical plumes are well parametrized by Monin–Obukhov theory, whereas large–scale circulatory motions obey to a different scaling. In this respect, Panofsky *et al.* (1977) pointed out that the correct scale for horizontal velocity fluctuations is probably the one defined by Deardorff (1970), namely $v_D = (\beta g Q h)^{1/3}$, which corresponds to Prandtl’s free-fall scale based on the channel height. Assuming $\overline{u'^2}^{1/2} \sim v_D$ implies $\overline{u'^2}^{1/2}/u_\tau \sim (h/L)^{1/3}$, hence explaining why the global trend of the streamwise velocity fluctuations with y/L is increasing, whereas the individual profiles are decreasing with y (also recalling the discussion made on figure 10c). In this context it is quite surprising that the u – θ correlation (panel (e)) satisfies the expected $-2/3$ scaling law in the free-convection regime (Kader & Yaglom 1990), whereas the individual profiles have strong scatter under conditions of near-neutral stratification.

6. Parametrization of heat transfer and skin friction

The prediction of heat transfer and aerodynamic drag under conditions of unstable stratification is a topic of obvious interest in engineering and meteorology. Given the absence of reliable theoretical mean temperature and velocity profiles for flow conditions far from neutral (Scagliarini *et al.* 2015), we attempt to derive correlations based on the available DNS data. For that purpose, we preliminarily try to gain a perception for the behavior of heat transfer and friction coefficients as a function of the governing parameters. In figure 16 we show the computed Nusselt number, defined as

$$Nu = \frac{2Qh}{\alpha\Delta\theta}, \quad (6.1)$$

as a function of the Rayleigh number, grouped into curves at constant Reynolds number (a) and constant Richardson number (b). Data are compensated by $Ra^{0.3}$ to better highlight scatter among curves. Panel (a) shows that data at sufficiently high Ra tend to cluster around the free-convection ($Ra = \infty$) distribution, with departures taking place at higher Ra as the Reynolds number increases, suggesting that the Richardson number may be an important parameter to distinguish among different cases. The figure also shows that the Nusselt number is not a monotonic function of Re_b for fixed Ra , with the counterintuitive conclusion that some small amount of forced convection may yield reduction of the heat exchange with respect to the pure buoyant case, as also evident in panel (b). This effect is the likely consequence of sweeping of convective plumes by large-scale motions, with subsequent loss of efficiency in heat redistribution (Scagliarini

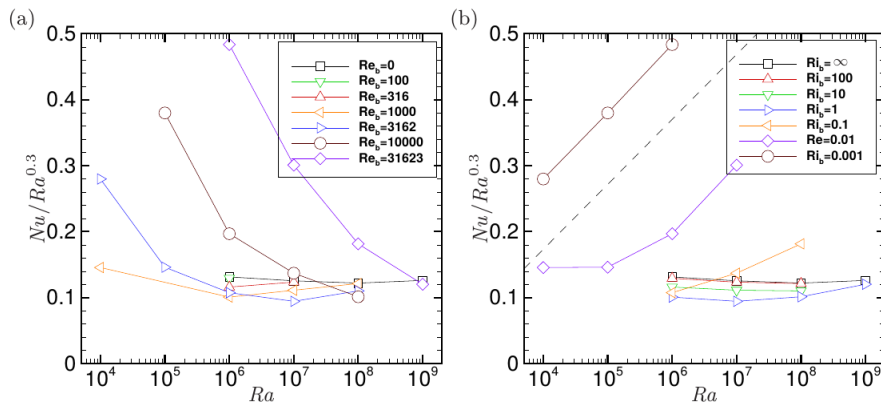


Figure 16: Compensated distributions of Nusselt number as a function of Rayleigh number, grouped into lines with same Re_b (a) and with same Ri_b (b). The dashed line in panel (b) indicates a $Ra^{0.45}$ power law.

et al. 2014). Fitting the DNS data in the free-convection regime we obtain

$$Nu(Ra) \approx 0.1165 Ra^{0.304}, \quad (6.2)$$

with a power-law exponent not too far from that typically reported in this range of relatively low Ra (Ahlers *et al.* 2009; Orlandi *et al.* 2015b). The effect of Richardson number reduction from pure buoyancy (see figure 16b) is initially a downward translation of the $Nu(Ra)$ curve, with maximum reduction of up to 20% at $Ri_b = 1$. Further reduction of Ri_b yields a marked increase in the slope of the $Nu(Ra)$ curve, which tends to attain a $Ra^{0.45}$ slope in the forced convection limit. Fitting the DNS data herein reported in the $Ri_b = 0$ limit as well as data at higher Re_b (Pirozzoli *et al.* 2016) yields

$$Nu(Re_b) \approx 0.0073 Re_b^{0.802}. \quad (6.3)$$

A typical engineering approach (Bergman *et al.* 2011) consists of using either equation (6.2) if $Ri_b \gtrsim 1$ or equation (6.3) if $Ri_b \lesssim 1$. A convex combination of the two formulas is also sometimes used

$$Nu(Ra, Re_b) = (Nu(Ra)^n + Nu(Re_b)^n)^{1/n}, \quad (6.4)$$

with $n \approx 3$. The performance of equation (6.4), with the limit Nusselt distributions given in equations (6.2) (6.3) is tested in figure 18(a) against a comparison with the DNS data in the mixed convection regime. The agreement seems to be fair in the whole parameter space covered by the simulations, although the formula cannot obviously capture the previously noticed slight Nusselt with Re_b which is observed mainly around unity bulk Richardson number.

The distribution of the friction coefficients, defined as

$$C_f = 2\tau_w/(\rho u_b^2), \quad (6.5)$$

is shown in figure 17, grouped into curves with constant Ra (a) and with constant Ri_b (b). For the sake of reference, in the figure we also show the friction curve for laminar channel flow, and Prandtl's turbulent friction law, derived by solving the equation

$$\sqrt{\frac{2}{C_f(Re_b)}} = \frac{1}{k} \log \left(\frac{Re_b}{2} \sqrt{\frac{C_f(Re_b)}{2}} \right) + C - \frac{1}{k}, \quad (6.6)$$

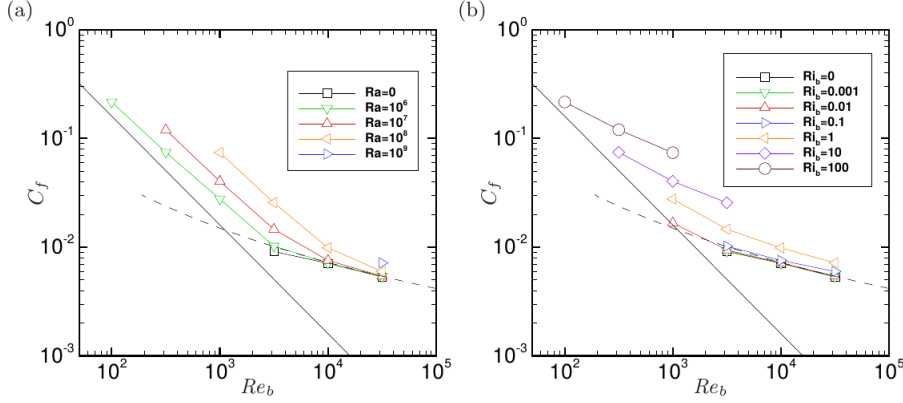


Figure 17: Distributions of friction coefficient as a function of Reynolds number, grouped into lines with same Ra (a) and with same Ri_b (b). The solid and dashed lines in (b) indicate the laminar Poiseuille curve $C_f = 16/Re_b$, and Prandtl's friction law for turbulent channels (equation (6.6)), respectively.

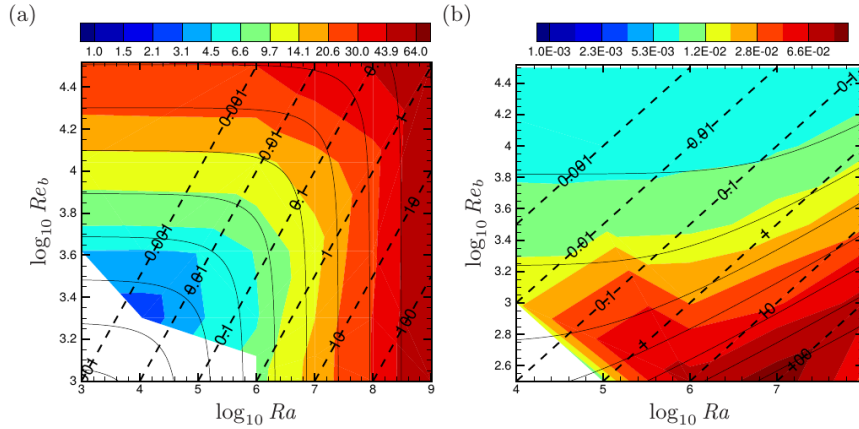


Figure 18: Maps of Nusselt number (a) and friction coefficient (b) as a function of Rayleigh and Reynolds number. The colored contours correspond to the DNS data, whereas the solid lines indicates fits obtained from equations (6.4),(6.7). The dashed diagonal lines have constant Ri_b . Twelve logarithmically-spaced contour levels are shown for each variable, with $1 \leq Nu \leq 64$, $0.001 \leq C_f \leq 0.1$.

with $k = 0.383$, $C = 4.17$ (Pirozzoli *et al.* 2014). We find (panel (a)) that increasing the Rayleigh number consistently yields an increase of C_f , which however tends to saturate at high Re_b . In the low- Re_b limit the friction curves appear to be nearly parallel to the laminar curve, although the Ra -dependent displacement suggest that the structure of the velocity field is different from the classical Poiseuille representation, as we previously pointed out. The same data reported at constant Ri_b in panel (b) show a steady upward displacement of the friction curves with Ri_b , which is suggestive of a possible parametrization of the friction coefficient in the form

$$C_f(Ra, Re_b) = C_f(Re_b) + \Delta C_f(Ri_b), \quad (6.7)$$

with $C_f(Re_b)$ given in equation (6.6). Fitting the DNS data we obtain the following empirical representation for the correction due to buoyancy

$$\Delta C_f(Ri_b) = (1 + 2Ri_b)^{0.3}. \quad (6.8)$$

The performance of the predictive formulas (6.7)+(6.8) can be appreciated in figure 18(b), where C_f is shown in the $Ra-Re_b$ plane. It appears that this simple parametrization correctly captures the increasing trend of C_f in the presence of finite buoyancy, although quantitative agreement with DNS data is not perfect under all flow regimes.

7. Conclusions

We have carried out direct numerical simulations of turbulent channel flows with unstable thermal stratification in a wide range of Reynolds and Rayleigh numbers varying between the extreme cases of pure free and forced convection. Concerning the large-scale structures, the most interesting effect of mixed convection is the formation of quasi-longitudinal rollers which fill the entire channel height, and whose spanwise aspect-ratio may be very large, probably depending to some extent on the size of the computational box. It is worthwhile noting that this effect, absent in pure Rayleigh-Bénard convection and in the turbulent channel flow, shows-up for a wide range of Richardson numbers (based on DNS data, we find at least $0.01 \leq Ri_b \leq 100$), hence virtually in all situations where mixed convection is relevant. The core rollers can be interpreted as the turbulent counterpart of Rayleigh instability modes, which become ordered under the action of the mean shear. It should be noted, however, that the laminar rollers have a typical aspect-ratio of unity, whereas turbulent rollers are typically much more oblate. Another interesting feature of turbulent rollers is their tendency to meander in the spanwise direction, again in a fashion reminiscent of the wavy secondary instabilities of laminar rollers. Maximum meandering seems to occur at $Ri_b \approx 1$, whereas maximum ordering is found in conditions close to pure forced convection, namely $Ri_b \approx 0.01$. The near-wall flow organization consists of the typical pattern of thermal plumes at $Ri_b \gtrsim 1$, and of momentum streaks at $Ri_b \lesssim 1$, with strong modulating influence from the core rollers.

While the flow statistics are well understood in the case of pure forced convection, things are not clear-cut as the limit of free convection is approached. Specifically, in-depth analysis of the flow statistics shows that the mean temperature is far from the $y^{-1/3}$ scaling predicted by Prandtl based on the assumption that the flow is dominated by wall-attached plumes. Reasons for this discrepancy may be related to the importance of the core rollers in global redistribution of temperature which destroy strict wall scaling. Based on the present dataset, however, we cannot rule out the possibility that Prandtl's scaling only emerges at Rayleigh numbers much higher than those considered in this paper and currently accessible to DNS. The same arguments are likely to apply to the horizontal velocity fluctuations, whose variance is decreasing with the wall distance, rather than increasing according to $y^{2/3}$ as required by plume-based scaling. On the other hand, vertical velocity and temperature fluctuations closely conform to the model predictions, hence suggesting that vertical motions are mainly controlled by thermal plumes. These findings have large impact on classical parametrizations of heat flux and wall friction, mainly based on the Monin-Obukhov dimensional ansatz that wall-scaled mean flow gradients and fluctuations should be universal functions of y/L . Based on the present DNS database, we find that this assumption is satisfied with reasonable accuracy, probably acceptable for 'first-order' estimates. However, we also find that the predictive accuracy of empirical formulas relying on Monin-Obukhov universality varies considerably depending on the variables. Specifically, we find that the individual profiles

of vertical velocity, temperature variance and the u - θ correlation follow quite well the universal trends. On the other hand, the profiles of mean temperature and velocity as well as the horizontal velocity variances only follow the theoretical trends in a global sense, whereas individual profiles show a radically different behaviour. This is likely to result from the coexistence of a plume-dominated scaling with statistics varying with y/L , and a core-dominated scaling, with quantities scaling as h/L Panofsky *et al.* (1977). Direct verification of this inference would require simulations covering individually a wide range of y/L , which is only possible using simultaneously extreme values of Ra , Re_b , and certainly beyond the current DNS capabilities. An relevant outcome of the present study is a set of modified Businger–Dyer relationships for the various flow variables based on fitting the DNS data. Differences with curve fits of current use in meteorological parametrizations are generally small, except for the mean streamwise velocity, for which we recover a very mild $(y/L)^{-1/7}$ variation in the light wind regime, which is sensibly different from the $(y/L)^{-1/4}$ of current use. This finding is potentially interesting as correct parametrization of the light-wind regime can have large impact on the prediction of weather conditions featuring strong thermal instability, as is the case of the Indian monsoon circulation (Rao & Narasimha 2006). The present DNS data are especially important for this purpose, as mean wind data in the light wind regime are extremely scattered owing to difficulties inherent to field atmospheric measurements. We should however also recall that the high- Ri_b regime is particularly challenging also for DNS, as it corresponds to the bottom-right corner of figure 1, where Rayleigh numbers are high but Reynolds number are rather low, thus possibly casting uncertainties on direct applicability of DNS data to the context of atmospheric turbulence.

Of large practical interest is also the prediction of friction and heat transfer as a function of the bulk flow parameters. Regarding heat transfer, a peculiar behavior is observed whereby the addition of bulk mass flow initially leads to a decrease of the Nusselt number down to $Ri_b \approx 1$, and then an increase moving toward the forced convection regime. Reasonable estimates for Nu , which however do not incorporate this effect are obtained by simple geometric averages of the values found in the limits of free and forced convection. Empirical corrections to the classical heat transfer formulas valid for neutral channels are also established to incorporate the effect of buoyancy by fitting the DNS data. A simple parametrization based on the sole bulk Richardson number yields predictions with $O(10\%)$ accuracy in the whole Ra , Re_b parameter space.

This work was carried out on the national e-infrastructure of SURFsara, a subsidiary of SURF cooperation, the collaborative ICT organization for Dutch education and research. We also acknowledge PRACE for awarding us access to FERMI based in Italy at CINECA under PRACE project numbers 2015133124 and 2015133204. We also acknowledge that the results of this research have been achieved using the DECI resource Archer based in the United Kingdom at Edinburgh with support from the PRACE aisbl.

REFERENCES

- ABE, H. & ANTONIA, R.A. 2009 Near-wall similarity between velocity and scalar fluctuations in a turbulent channel flow. *Phys. Fluids* **21**, 025109.
- AHLERS, G, GROSSMANN, S & LOHSE, D 2009 Heat transfer and large scale dynamics in turbulent rayleigh-bénard convection. *Rev. Mod. Phys.* **81** (2), 503.
- AHLERS, G., HE, X., FUNFSCHILLING, D. & BODENSCHATZ, E. 2012 Heat transport by turbulent Rayleigh-Bénard convection for $Pr \simeq 0.8$ and $3 \times 10^{12} \leq Ra \leq 10^{15}$: Aspect ratio $\gamma = 0.50$. *New J. Phys.* **14**, 103012.

- ARMENIO, V. & SARKAR, S. 2002 An investigation of stably stratified turbulent channel flow using large-eddy simulation. *J. Fluid Mech.* **459**, 1–42.
- AVSEC, D 1937 Sur les formes ondulées des tourbillons en bandes longitudinales. *C. R. Acad. Sci. Paris* **204**, 167–169.
- AVSEC, D & LUNTZ, M 1937 Tourbillons thermoconvectifs et électroconvectifs. *La Météorologie* **31**, 180–194.
- BÉNARD, H & AVSEC, D 1938 Travaux récents sur les tourbillons cellulaires et les tourbillons en bandes. Applications à l’astrophysique et à la météorologie. *J. Phys. Radium* **9** (11), 486–500.
- BERGMAN, T.L., LAVINE, A.S., INCROPERA, F.P. & DEWITT, D.P. 2011 *Introduction to heat transfer*. John Wiley & Sons.
- BERNARDINI, M, PIROZZOLI, S & ORLANDI, P 2014 Velocity statistics in turbulent channel flow up to $Re_\tau = 4000$. *J. Fluid Mech.* **742**, 171–191.
- BROWN, R.A. 1980 Longitudinal instabilities and secondary flows in the planetary boundary layer: A review. *Rev. Geophys.* **18** (3), 683–697.
- BUSINGER, JA, WYNGAARD, JC, IZUMI, Y & BRADLEY, EF 1971 Flux-profile relationships in the atmospheric surface layer. *J. Atmos. Sci.* **28** (2), 181–189.
- CEBECI, T. & BRADSHAW, P. 1984 *Physical and computational aspects of convective heat transfer*. Springer-Verlag, New York, NY.
- CLEVER, RM & BUSSE, FH 1991 Instabilities of longitudinal rolls in the presence of Poiseuille flow. *J. Fluid Mech.* **229**, 517–529.
- CLEVER, RM & BUSSE, FH 1992 Three-dimensional convection in a horizontal fluid layer subjected to a constant shear. *J. Fluid Mech.* **234**, 511–527.
- DEARDORFF, JW 1970 Convective velocity and temperature scales for the unstable planetary boundary layer and for Rayleigh convection. *J. Atmos. Sci.* **27** (8), 1211–1213.
- DEARDORFF, JW 1972 Numerical investigation of neutral and unstable planetary boundary layers. *J. Atmos. Sci.* **29** (1), 91–115.
- DOMARADZKI, J ANDRZEJ & METCALFE, RW 1988 Direct numerical simulations of the effects of shear on turbulent Rayleigh-Bénard convection. *J. Fluid Mech.* **193**, 499–531.
- DYER, AJ 1974 A review of flux-profile relationships. *Bound.-Lay. Meteorol.* **7** (3), 363–372.
- FUKUI, K. & NAKAJIMA, M. 1985 Unstable stratification effects on turbulent shear flow in the wall region. *Int. J. Heat Mass Transfer* **28** (12), 2343–2352.
- FUKUI, K., NAKAJIMA, M. & UEDA, H. 1991 Coherent structure of turbulent longitudinal vortices in unstably-stratified turbulent flow. *Int. J. Heat Mass Transfer* **34** (9), 2373–2385.
- GAGE, KS & REID, WH 1968 The stability of thermally stratified plane Poiseuille flow. *J. Fluid Mech.* **33** (01), 21–32.
- GARCIA-VILLALBA, M. & ALAMO, J.C. DEL 2011 Turbulence modification by stable stratification in channel flow. *Phys. Fluids* **23** (4), 045104.
- HAINES, D.A. 1982 Horizontal roll vortices and crown fires. *J. Appl. Meteor.* **21** (6), 751–763.
- HAMMAN, C & MOIN, P 2015 Thermal convection from a minimal flow unit to a wide fluid layer. *B. Am. Phys. Soc.* **60**.
- HANNA, S.R. 1969 The formation of longitudinal sand dunes by large helical eddies in the atmosphere. *J. Appl. Meteor.* **8** (6), 874–883.
- HILL, G.E. 1968 On the orientation of cloud bands. *Tellus* **20** (1), 132–137.
- IDA, O & KASAGI, N 1997 Direct numerical simulation of unstably stratified turbulent channel flow. *ASME J. Heat Transfer* **119** (1), 53–61.
- JIMÉNEZ, J., WRAY, A. A., SAFFMAN, P. G. & ROGALLO, R. S. 1993 The structure of intense vorticity in isotropic turbulence. *J. Fluid Mech.* **255**, 65–90.
- JOHANSSON, C, SMEDMAN, A-S, HÖGSTRÖM, U, BRASSEUR, JG & KHANNA, S 2001 Critical test of the validity of Monin-Obukhov similarity during convective conditions. *J. Atmos. Sci.* **58** (12), 1549–1566.
- KADER, B.A. 1981 Temperature and concentration profiles in fully turbulent boundary layers. *Int. J. Heat Mass Transfer* **24**, 1541–1544.
- KADER, BA & YAGLOM, AM 1990 Mean fields and fluctuation moments in unstably stratified turbulent boundary layers. *J. Fluid Mech.* **212**, 637–662.

- KAYS, W.M., CRAWFORD, M.E. & WEIGAND, B. 1980 *Convective heat and mass transfer*. McGraw-Hill.
- KERR, RM 1996 Rayleigh number scaling in numerical convection. *J. Fluid Mech.* **310**, 139–179.
- KHANNA, S & BRASSEUR, JG 1997 Analysis of Monin-Obukhov similarity from large-eddy simulation. *J. Fluid Mech.* **345**, 251–286.
- KHANNA, S & BRASSEUR, JG 1998 Three-dimensional buoyancy-and shear-induced local structure of the atmospheric boundary layer. *J. Atmos. Sci.* **55** (5), 710–743.
- KIM, J., MOIN, P. & MOSER, R.D. 1987 Turbulence statistics in fully developed channel flow at low Reynolds number. *J. Fluid Mech.* **177**, 133–166.
- KUETTNER, J.P. 1959 The band structure of the atmosphere. *Tellus* **11** (3), 267–294.
- KUETTNER, J.P. 1971 Cloud bands in the earth’s atmosphere: Observations and theory. *Tellus* **23** (4-5).
- LEE, M. & MOSER, R.D. 2015 Direct simulation of turbulent channel flow layer up to $Re_\tau = 5200$. *J. Fluid Mech.* **774**, 395–415.
- MAL, S. 1930 Forms of stratified clouds. *Beitr. Phys. Atmos* **17**, 40–68.
- MIZUSHINA, T., OGINO, F. & KATADA, N. 1982 Ordered motion of turbulence in a thermally stratified flow under unstable conditions. *Int. J. Heat Mass Transfer* **25** (9), 1419–1425.
- MONIN, AS & OBUKHOV, AM 1954 Basic laws of turbulent mixing in the surface layer of the atmosphere. *Contrib. Geophys. Inst. Acad. Sci. USSR* **151**, 163–187.
- NIEMELA, J.J., SKRBEK, L., SREENIVASAN, K.R. & DONNELLY, R.J. 2000 Turbulent convection at very high Rayleigh numbers. *Nature* **404**, 837–840.
- OBUKHOV, AM 1946 Turbulence in the atmosphere with inhomogeneous temperature. *Trudy Geofiz. Inst. AN SSSR* **1**.
- ORLANDI, P., BERNARDINI, M. & PIROZZOLI, S. 2015a Poiseuille and Couette flows in the transitional and fully turbulent regime. *J. Fluid Mech.* pp. 424–441.
- ORLANDI, P, PIROZZOLI, S & BERNARDINI, M 2015b Influence of wall roughness and thermal conductivity on turbulent natural convection. *B. Am. Phys. Soc.* **60**.
- PABIOU, H., MERGUI, S. & BENARD, C. 2005 Wavy secondary instability of longitudinal rolls in Rayleigh–Bénard–Poiseuille flows. *J. Fluid Mech.* **542**, 175–194.
- PANOFSKY, HA, TENNEKES, H, LENSCHOW, DH & WYNGAARD, JC 1977 The characteristics of turbulent velocity components in the surface layer under convective conditions. *Bound.-Lay. Meteorol.* **11** (3), 355–361.
- PAULSON, CA 1970 The mathematical representation of wind speed and temperature profiles in the unstable atmospheric surface layer. *J. Appl. Meteor.* **9** (6), 857–861.
- PIROZZOLI, S., BERNARDINI, M. & ORLANDI, P. 2014 Turbulence statistics in Couette flow at high Reynolds number. *J. Fluid Mech.* **758**, 327–343.
- PIROZZOLI, S, BERNARDINI, M & ORLANDI, P 2016 Passive scalars in turbulent channel flow at high Reynolds number. *J. Fluid Mech.* **788**, 614–639.
- PRANDTL, L 1932 Meteorologische anwendung der strömungslehre. *Beitr. Phys. Atmos* **19**, 188–202.
- RAO, KG 2004 Estimation of the exchange coefficient of heat during low wind convective conditions. *Bound.-Lay. Meteorol.* **111** (2), 247–273.
- RAO, KG & NARASIMHA, R 2006 Heat-flux scaling for weakly forced turbulent convection in the atmosphere. *J. Fluid Mech.* **547**, 115–135.
- SCAGLIARINI, A, EINARSSON, H, GYLFASON, Á & TOSCHI, F 2015 Law of the wall in an unstably stratified turbulent channel flow. *J. Fluid Mech.* **781**, R5.
- SCAGLIARINI, A, GYLFASON, Á & TOSCHI, F 2014 Heat-flux scaling in turbulent Rayleigh–Bénard convection with an imposed longitudinal wind. *Phys. Rev. E* **89** (4), 043012.
- SHISHKINA, O, STEVENS, RJAM, GROSSMANN, S & LOHSE, D 2010 Boundary layer structure in turbulent thermal convection and its consequences for the required numerical resolution. *New J. Phys.* **12** (7), 075022.
- SID, S, DUBIEF, Y & TERRAPON, V 2015 Direct numerical simulation of mixed convection in turbulent channel flow: On the Reynolds number dependency of momentum and heat transfer under unstable stratification. In *Proc. 8th International Conference on Computational Heat and Mass Transfer*, p. 190. Istanbul, Turkey.
- STEVENS, R.J.A.M., LOHSE, D. & VERZICCO, R. 2011 Prandtl and Rayleigh number depen-

- dence of heat transport in high Rayleigh number thermal convection. *J. Fluid Mech.* **688**, 31–43.
- STULL, RB 2012 *An introduction to boundary layer meteorology*, , vol. 13. Springer Science & Business Media.
- WYNGAARD, JC 1992 Atmospheric turbulence. *Annu. Rev. Fluid Mech.* **24** (1), 205–234.
- ZONTA, FRANCESCO ???? Nusselt number and friction factor in thermally stratified turbulent channel flow under non-Oberbeck–Boussinesq conditions .
- ZONTA, F & SOLDATI, A 2014 Effect of temperature dependent fluid properties on heat transfer in turbulent mixed convection. *ASME J. Heat Transfer* **136** (2), 022501.